The role of meso-scale structures in rapid gas–solid flows

By KAPIL AGRAWAL[1], PETER N. LOEZOS[1],
MADHAVA SYAMLAL[2]
AND SANKARAN SUNDARESAN[1]†

[1]Department of Chemical Engineering, Princeton University, Princeton, NJ 08544, USA
[2]Fluent Inc., P.O. Box 880, Morgantown, WV 26507-0880, USA

Meso-scale structures that take the form of clusters and streamers are commonly observed in dilute gas–particle flows, such as those encountered in risers. Continuum equations for gas–particle flows, coupled with constitutive equations for particle-phase stress deduced from kinetic theory of granular materials, can capture the formation of such meso-scale structures. These structures arise as a result of an inertial instability associated with the relative motion between the gas and particle phases, and an instability due to damping of the fluctuating motion of particles by the interstitial fluid and inelastic collisions between particles. It is demonstrated that the meso-scale structures are too small, and hence too expensive, to be resolved completely in simulation of gas–particle flows in large process vessels. At the same time, failure to resolve completely the meso-scale structures in a simulation leads to grossly inaccurate estimates of inter-phase drag, production/dissipation of pseudo-thermal energy associated with particle fluctuations, the effective particle-phase pressure and the effective viscosities. It is established that coarse-grid simulation of gas–particle flows must include sub-grid models, to account for the effects of the unresolved meso-scale structures. An approach to developing a plausible sub-grid model is proposed.

1. Introduction

Experimental studies on high-velocity gas–particle flows in vertical pipes have revealed that particles are usually distributed over the cross-section of the pipe in a non-uniform fashion (e.g. see Weinstein, Shao & Schnitzlein 1986; Bader, Findlay & Knowlton 1988). This non-uniformity may introduce downflow of particles and gas in some regions, usually near the pipe wall, even though the cross-sectional average flows of particles and gas are upward. Riser flows are inherently unsteady with large fluctuations in suspension density (Schnitzlein & Weinstein 1988). It is now well established that meso-scale structures, namely clusters and streamers of particles, whose characteristic size is on the order of 10–100 particle diameters, are present in such flows (Grace & Tuot 1979; Gidaspow 1994; Horio 1995; Tsukada 1995). These structures affect the overall flow behaviour significantly and should therefore be accounted for in computational fluid dynamic (CFD) simulations of riser flows.

† Author to whom correspondence should be addressed: sundar@princeton.edu

Unfortunately, the meso-scale structures cannot be adequately resolved in CFD simulations of typically sized risers. It will be demonstrated in this paper that a sub-grid model to account for the effect of the unresolved meso-scale structures must be developed and incorporated into the coarse-grid simulations. Small-scale structures in gas–particle flows arise because of local instabilities and macro-scale shear is not necessary to induce them. Macro-scale shear modifies the small-scale structures and produces anisotropic normal stresses and a shear-thinning behaviour.

A brief review of the evolution of continuum models for riser flows is presented in §2. The origin of meso-scale structures is discussed in §3, where we show that continuum models based on the kinetic theory of granular materials (for example, see Gidaspow 1994) do contain the essential physics needed to capture the clusters and streamers in a qualitatively correct manner. The various routes to cluster formation are discussed in §4, where we argue that these structures arise as a result of two mechanisms operating in parallel: an instability due to damping of the fluctuating motion of particles by the interstitial fluid and inelastic collisions between particles and an inertial instability associated with gas–particle slip.

In §5, we demonstrate that coarse-grid simulations which fail to recognize the sub-grid microstructure (i.e. small clusters and streamers) overestimate the drag force and underestimate the rate of production and dissipation of pseudo-thermal energy, effective viscosities of the gas and particle phases and the effective normal stress in the particle phase. An approach to developing a sub-grid model for coarse-grid simulation of gas–particle flow in risers is also described.

2. Continuum modelling of gas–solid flows

Model equations

The total number of particles typically present in most gas–particle flows of practical interest is extremely large, making it impractical to solve for the motion of each particle. Consequently, gas–particle flows in large process units are usually modelled via averaged equations of motion (Anderson & Jackson 1967). The model equations we work with in this paper are given in table 1. Equations (1)–(4) are the continuity and momentum balance equations for the particle and gas phases. Here, ϕ is the volume fraction of particles; v and u are the local average velocities of the particle and gas phases, respectively; ρ_s and ρ_g are the densities; σ_s and σ_g are the stress tensors associated with the two phases expressed in a compressive sense; f is the interaction force between the phases per unit volume of the bed; and g is the specific gravity force.

The concentration of particles in riser flows is sufficiently large that direct inter-action of particles through collisions occurs easily and rapidly. In such situations, it is now common to invoke the kinetic theory of granular materials to close the solids-phase stress (Sinclair & Jackson 1989). This closure requires that we augment the above equations with a balance of pseudo-thermal energy (PTE) of particle vel-ocity fluctuations as the solids phase stress depends directly on this quantity (e.g. see Lun *et al.* 1984; Gidaspow 1994). Equation (5) represents the PTE balance, where T denotes the granular temperature. The first term on the right-hand side of this equation represents the diffusive transport of PTE, with q denoting the diffusive flux of PTE. The second and third terms represent rates of production of PTE by shear and gas–particle slip, respectively. The fourth and the fifth terms denote rates of dissipation of PTE through inelastic collisions and viscous damping, respectively.

$$\frac{\partial \phi}{\partial t} + \nabla \cdot (\phi \boldsymbol{v}) = 0, \tag{1}$$

$$\frac{\partial (1 - \phi)}{\partial t} + \nabla \cdot [(1 - \phi)\boldsymbol{u}] = 0, \tag{2}$$

$$\left[\frac{\partial (\rho_s \phi \boldsymbol{v})}{\partial t} + \nabla \cdot (\rho_s \phi \boldsymbol{v}\boldsymbol{v}) \right] = -\nabla \cdot \boldsymbol{\sigma}_s - \phi \nabla \cdot \boldsymbol{\sigma}_g + \boldsymbol{f} + \rho_s \phi \boldsymbol{g}, \tag{3}$$

$$\left[\frac{\partial (\rho_g (1 - \phi)\boldsymbol{u})}{\partial t} + \nabla \cdot (\rho_g (1 - \phi)\boldsymbol{u}\boldsymbol{u}) \right] = -(1 - \phi)\nabla \cdot \boldsymbol{\sigma}_g - \boldsymbol{f} + \rho_g (1 - \phi)\boldsymbol{g}, \tag{4}$$

$$\left[\frac{\partial \left(\frac{3}{2} \rho_s \phi T \right)}{\partial t} + \nabla \cdot \left(\frac{3}{2} \rho_s \phi T \boldsymbol{v} \right) \right] = -\nabla \cdot \boldsymbol{q} - \boldsymbol{\sigma}_s : \nabla \boldsymbol{v} + \Gamma_{slip} - J_{coll} - J_{vis}. \tag{5}$$

Gas-phase stress tensor

$$\boldsymbol{\sigma}_g = p_g \boldsymbol{I} - \hat{\mu}_g \left[\nabla \boldsymbol{u} + (\nabla \boldsymbol{u})^T - \frac{2}{3}(\nabla \cdot \boldsymbol{u})\boldsymbol{I} \right]. \tag{6}$$

Gas-particle drag (Gidaspow 1994)

$$\boldsymbol{f} = \beta(\boldsymbol{u} - \boldsymbol{v}), \quad \beta = \frac{3}{4} C_D \frac{\rho_g (1 - \phi)\phi|\boldsymbol{u} - \boldsymbol{v}|}{d} F(\phi), \quad F(\phi) = (1 - \phi)^{-2.65}, \tag{7}$$

$$C_D = \begin{cases} (24/Re_g)(1 + 0.15Re_g^{0.687}), & Re_g < 1000 \\ 0.44, & Re_g \geqslant 1000, \end{cases} \quad Re_g = \frac{(1 - \phi)\rho_g d|\boldsymbol{u} - \boldsymbol{v}|}{\mu_g}. \tag{8}$$

Solids stress

$$\boldsymbol{\sigma}_s = [\rho_s \phi(1 + 4\eta\phi g_o)T - \eta\mu_b(\nabla \cdot \boldsymbol{v})]\boldsymbol{I}$$
$$- \left(\frac{2 + \alpha}{3} \right) \left\{ \frac{2\mu^*}{g_o \eta(2 - \eta)} (1 + \frac{8}{5}\phi\eta g_o)(1 + \frac{8}{5}\eta(3\eta - 2)\phi g_o) + \frac{6}{5}\eta\mu_b \right\} \boldsymbol{S}. \tag{9}$$

Pseudo-thermal energy flux vector

$$\boldsymbol{q} = -\frac{\lambda^*}{g_o} \left\{ \left(1 + \frac{12}{5}\eta\phi g_o \right) \left(1 + \frac{12}{5}\eta^2(4\eta - 3)\phi g_o \right) + \frac{64}{25\pi}(41 - 33\eta)\eta^2\phi^2 g_o^2 \right\} \nabla T, \tag{10}$$

$$\boldsymbol{S} = \frac{1}{2}(\nabla \boldsymbol{v} + (\nabla \boldsymbol{v})^T) - \frac{1}{3}(\nabla \cdot \boldsymbol{v})\boldsymbol{I}. \tag{11}$$

Rate of dissipation of pseudo-thermal energy

$$J_{coll} = \frac{48}{\sqrt{\pi}} \eta(1 - \eta) \frac{\rho_s \phi^2}{d} g_o T^{3/2}, \tag{12}$$

$$\mu^* = \frac{\mu}{1 + \frac{2\beta\mu}{(\rho_s\phi)^2 g_o T}}, \quad \lambda^* = \frac{\lambda}{1 + \frac{6\beta\lambda}{5(\rho_s\phi)^2 g_o T}}, \tag{13}$$

$$\mu = \frac{5\rho_s d\sqrt{\pi T}}{96}, \quad \mu_b = \frac{256\mu\phi^2 g_o}{5\pi}, \quad \lambda = \frac{75\rho_s d\sqrt{\pi T}}{48\eta(41 - 33\eta)}, \quad \eta = \frac{(1 + e_p)}{2}, \tag{14}$$

$$g_o = \frac{1}{1 - (\phi/\phi_{max})^{1/3}}, \quad \phi_{max} = 0.65, \quad \alpha = 1.6, \tag{15}$$

$$J_{vis} = 3\beta T, \quad \Gamma_{slip} = \frac{81\phi\mu_g^2|\boldsymbol{u} - \boldsymbol{v}|^2}{g_o d^3 \rho_s \sqrt{\pi T}}. \tag{16}$$

Boundary conditions for particulate phase (Johnson & Jackson 1987)

$$\boldsymbol{n} \cdot \boldsymbol{\sigma}_s \cdot \boldsymbol{t} + \frac{\pi}{2\sqrt{3}\phi_{max}} \phi' \rho_s \phi g_o T^{1/2} \boldsymbol{v}_{sl} = 0, \tag{17}$$

$$\boldsymbol{n} \cdot \boldsymbol{q} = \frac{\pi\sqrt{3}}{6\phi_{max}} \phi' \rho_s \phi g_o T^{1/2} |\boldsymbol{v}_{sl}|^2 - \frac{\pi\sqrt{3}}{4\phi_{max}} (1 - e_w^2)\rho_s \phi g_o T^{3/2}, \tag{18}$$

$$\boldsymbol{v}_{sl} = \boldsymbol{v} - \boldsymbol{v}_w.$$

TABLE 1. Model equations for gas–particle flows.

The solids-phase stress, the PTE flux and the rate of dissipation of PTE due to inelastic collisions are expressed in a manner very similar to that proposed by Lun *et al.* (1984), see (9)–(15). The particles are assumed to be smooth hard spheres of diameter d and only binary interactions (characterized by a single parameter, namely the coefficient of normal restitution, e_p) are considered. The role of the interstitial fluid was not considered by Lun *et al.* (1984), but has been studied by several researchers since (S. B. Savage 1987, personal communication; Koch 1990; Ma & Ahmadi 1988; Gidaspow 1994; Balzer, Boelle & Simonin 1995; Boelle, Balzer & Simonin 1995; Koch & Sangani 1999). Following Savage (1987), Ma & Ahmadi (1988), Balzer *et al.* (1995) and Boelle *et al.* (1995), we have accounted for the role of the interstitial fluid in these expressions through the terms μ^* and λ^*, see (13). The expressions for the granular viscosities (μ and μ_b) and thermal conductivity (λ) given in (14) are the same as those in Lun *et al.* (1984).

The rate of dissipation of PTE by viscous damping is modelled in most of our simulations following Gidaspow (1994), see (16). We will also present some results obtained using an alternative model for this term proposed by Koch & Sangani (1999),

$$
\left.
\begin{aligned}
J_{vis} &= \frac{54\phi\mu_g T}{d^2} R_{diss}, \\
R_{diss} &= 1 + \frac{3\phi^{1/2}}{\sqrt{2}} + \frac{135}{64}\phi \ln \phi + 11.26\phi(1 - 5.1\phi + 16.57\phi^2 - 21.77\phi^3) - \phi g_o \ln \varepsilon_m,
\end{aligned}
\right\}
$$

(19)

where $\varepsilon_m = 0.01$ and demonstrate that the major findings of our study are not sensitive to the differences between the two different choices for J_{vis}.

The expression shown in (16) for the rate of production of PTE by gas–particle slip, Γ_{slip}, without the g_o term appearing there, was derived by Koch (1990) for dilute systems. More recently, Koch & Sangani (1999) have proposed that

$$
\Gamma_{slip} = \frac{81\phi\mu_g^2|\boldsymbol{u} - \boldsymbol{v}|}{g_o d^3 \rho_s \sqrt{\pi T}} \Psi
$$

(20)

where

$$
\Psi = \frac{R_d^2}{(1 + 3.5\phi^{1/2} + 5.9\phi)},
$$

$$
R_d = \begin{cases} \dfrac{1 + 3(\phi/2)^{1/2} + (135/64)\phi \ln \phi + 17.14\phi}{1 + 0.681\phi - 8.48\phi^2 + 8.16\phi^3}, & \phi < 0.4 \\[2ex] \dfrac{10\phi}{(1 - \phi)^3} + 0.7, & \phi \geqslant 0.4. \end{cases}
$$

(21)

The expression for Γ_{slip} given in (16) simply corresponds to setting Ψ to unity. Most of our simulations are based on (16), and we will demonstrate that including the correction factor, Ψ changes the results quantitatively but not qualitatively.

Equation (6) is a simple Newtonian closure for the effective gas phase stress. In the regime investigated in the present study, $\rho_s\phi \gg \rho_g(1 - \phi)$, and the contribution due to the deviatoric part of the gas-phase stress is negligible. This will be demonstrated by considering several different models for the effective viscosity of the gas phase, $\hat{\mu}_g$.

In our analysis, it is assumed that the gas–particle interaction force, $\boldsymbol{f}$, is only due to drag. Equations (7) and (8) are the drag correlation used in our simulations (Wen

d	Particle diameter	7.5×10^{-3} cm
ρ_s	Solids density	1.5 g cm^{-3}
ρ_g	Gas density	1.3×10^{-3} g cm^{-3}
μ_g	Gas viscosity	1.8×10^{-4} g cm^{-1} s^{-1}

TABLE 2. Physical properties of gas and solids used in simulations.

& Yu 1966). It can be shown readily that this model for drag, when applied to the problem of uniform sedimentation of particles in a fluid, yields a Richardson–Zaki (1954) coefficient of 4.65 at low Reynolds number, $Re_p (= \rho_g v_t d / \mu)$ and 2.325 at high Re_p. Typical physical properties of systems considered in our study are shown in table 2. For such systems, $Re_p \sim O(1)$ and the drag coefficient estimated from (8) and (9) is not very different from

$$\frac{18\mu_g\phi(1-\phi)^{-2.65}}{d^2}.$$

As we will see later, in our simulations, $T^{1/2} \sim 0.1 v_t$, and hence the Stokes number (St), based on ρ_s, d, $T^{1/2}$ and μ_g (e.g. see Wylie & Koch 2000), is $O(10^2)$. At such large values of St, $\mu^* \sim \mu$, $\lambda^* \sim \lambda$. The Froude number, $Fr_p(= v_t^2/gd)$, is ~ 60 for the combination of physical parameters shown in table 2. It is well known that dense fluidized beds of such particles bubble (Wilhelm & Kwauk 1948).

We will demonstrate in this paper that this system of equations is able to capture the meso-scale structures in gas–solid flows in a qualitatively correct manner. To this end we will discuss in the next section previous work on this problem and trace the origin of these structures. It will become clear that the meso-scale structures are driven by inherent instabilities and not macro-scale shear associated with boundaries.

Most of the results discussed in this paper are concerned with simulations performed in spatially periodic domains. However, we will present a few simulation results to demonstrate that the meso-scale structures persist even in the presence of solid boundaries. At such solid boundaries, we cover a range of possible scenarios by considering three different choices of boundary conditions – no slip, free slip and partial slip. Partial slip boundary conditions for particle–wall interactions have been discussed in the literature by a number of researchers (for example, see Johnson & Jackson 1987; Jenkins 1992; Jenkins & Louge 1997; Jenkins & Richman 1986). As a simple example of partial slip boundary condition, we have employed (17) and (18) (table 1) proposed by Johnson & Jackson (1987), where e_w is the particle–wall coefficient of restitution and ϕ' is the specularity coefficient.

Upon casting these equations in a dimensionless form using ρ_s, v_t and v_t^2/g as characteristic density, velocity and length, respectively, the following dimensionless groups result: Re_p, Fr_p, ρ_g/ρ_s and $\hat{\mu}_g/\mu_g$. The analysis described in this paper is restricted to $Re_p \sim O(1)$ or smaller, $Fr_p \gg 1$ and $\rho_g/\rho_s \ll 1$, which is representative of most gas–particle flows encountered in risers, where we also have $St \gg 1$.

2.1. *Previous work on continuum models for riser flows*

Sinclair & Jackson (1989) examined whether the continuity and momentum equations for the two phases coupled with the pseudo-thermal energy balance equation ((1)–(5) in Table 1) can predict a non-uniform distribution of particles over the cross-section of a vertical pipe under steady and fully developed flow conditions. In their analysis, they neglected the possible consequences of persistent fluctuations and the presence

of clusters and streamers. This model was able to yield rather good agreement with experimental data under some restrictive assumptions about the dissipation of PTE (Sinclair & Jackson 1989; Pita & Sundaresan 1991, 1993; Yasuna *et al.* 1995). Louge, Mastorakos & Jenkins (1991) and Bolio & Sinclair (1995) expanded this model by adding the effect of gas-phase turbulence and found that even in very dilute particle-laden flows where the flow patterns are largely dictated by the turbulent gas flow, particle–particle interactions can play a significant role.

Dasgupta, Jackson & Sundaresan (1994) viewed the fluctuations associated with the clusters as 'particle phase turbulence' and derived time-averaged equations of motion for the fully developed flow of the two phases by Reynolds averaging equations (1)–(4). Their analysis revealed that particles are driven to regions having a low intensity of particle-phase velocity fluctuations from regions of high intensity at rates proportional to the gradients in the intensity of fluctuations. These authors employed a speculative K–ε model for the particle-phase turbulence in order to illustrate the occurrence of segregation. Hrenya & Sinclair (1997) have expanded this work by integrating kinetic theory for granular materials and a model for particle-phase turbulence. Collectively, these studies have helped establish that meso- and macro-scale fluctuations occurring on length scales much larger than that of individual particles must be included in any model for gas–particle flows designed to capture the non-uniform distribution of particles over the cross-section of the riser.

At the same time, various research groups (Enwald & Almstedt 1999; Enwald, Peirano & Almstedt 1997; Enwald *et al.* 1999; Nieuwland *et al.* 1995, 1996; Samuelsberg & Hjertager 1996; Tsuo & Gidaspow 1990; Gidaspow 1993, 1994) have pursued research on simulation of riser flows through direct numerical integration of the locally averaged equations. These simulations do reveal the presence of persistent fluctuations and particle clusters. Such an approach where one tries to capture the time-averaged flow patterns through transient integration of the locally averaged equations is computationally very intensive. Furthermore, the sheer size of the problem, and that of the duct through which the gas–particle mixture is flowing, necessitate the use of coarse grids in the numerical calculations. Such calculations reveal large-scale spatial patterns occurring on a length scale larger than the grid size. It will be shown in this paper that when one uses finer and finer meshes in an attempt to test for grid-size independence of the results, it is invariably found that the features of the flow continue to change at all length and time scales. Therefore, it is not always clear if the computed results are the true consequences of the differential equation models that one is trying to solve. An example to highlight the effect of grid size on the results will be presented later in this paper.

The effect of grid size reveals clearly that unresolved details of flow in a given simulation have an influence on the features occurring on a scale larger than the grid size. The lessons learned from these different attempts to model riser flow using volume-averaged equations of motion can be summarized as follows:

If one wishes to simulate the events occurring at meso- and macro-scale in their entirety, direct numerical integration of the governing equations is the obvious route; however, a fully resolved simulation where the results are independent of the grid size is yet to be demonstrated.

Spatial non-uniformities that are present in a time-averaged sense may be captured by a system of steady-state equations derived by time-averaging the volume-averaged equations of motion. The meso-scale structures and the macro-scale spatio-temporal patterns are erased through such an averaging procedure, but their consequences appear in the final equations as additional terms for which closure relations must be

postulated. K–ε models fall in this category. Although some progress has been made in this type of modelling approach, the reliability of these models for simulation of developing flows has not been validated.

Intermediate to these two approaches is the coarse-grid simulation of two-phase flow (the analogue of large-eddy simulation of single-phase turbulent flow), where one simulates spatial and spatio-temporal patterns occurring at the macro-scale, but accounts for the effects of meso-scale structures occurring at a scale smaller than the grid size through additional closure relations.

One can immediately recognize that the three approaches are practised in simulations of single-phase turbulent flow. The cascade of energy associated with fluctuations in single-phase flow and two-phase flow are very different. In the former the energy flow is predominantly from large scale to small scale, while in the latter it is more complicated. Meso-scale structures, such as clusters and streamers, form initially at small length and time scales and grow into larger scales, so there is almost certainly some energy flow from the very small scale to larger scales. One may also anticipate a flow of energy from large scale to smaller scales, just as in the case of single-phase flow. Understanding the origin and nature of clusters and streamers in riser flow of gas–particle mixtures will pave the way for the development of better closures for the correlations appearing in the Reynolds-averaged model and the coarse-grid simulation model, and will also help us determine the requirements for a fully resolved direct numerical integration of the locally averaged equations such as those summarized in Table 1.

3. Origin of clusters in gas–particle flows

Risers are most commonly encountered as components of circulating fluidized beds (CFBs) in industrial practice. The interaction of the various components of a CFB is known to give rise to instabilities which propagate through the loop. It is therefore useful to inquire if meso-scale structures such as clusters and streamers observed in risers are manifestations of local events or are directly attributable to phenomena associated with the entire loop. It is clear from experimental studies on the dynamics of gas–particle mixtures in a circulating fluidized bed (Srivastava *et al.* 1998; Zhang, Jiang & Fan 1998) that the loop instability manifested itself as low-frequency oscillations in pressure and hold-up. The propagation of this instability through the loop can be recognized from the pressure signals gathered at different locations in the loop. Zhang *et al.* (1998) have shown that the low-frequency components of the oscillations observed at different locations of their CFB apparatus were correlated, while the high-frequency components of the fluctuations (in pressure) at different locations were not. High-frequency fluctuations persist even under conditions where loop instability was not observed (Srivastava *et al.* 1998). It follows that clusters and streamers, which are most likely to be associated with the high-frequency fluctuations, arise from local processes and not because of the loop instability. It is therefore reasonable to conclude that the origin and nature of the clusters can be probed by considering a small segment of the riser.

3.1. *Riser flow simulations*

To probe the origin of clusters further, we performed two-dimensional simulations of gas–particle flow in a segment of a vertical channel, as described below. The MFIX code (Syamlal, Rogers & O'Brien 1993) was modified extensively for solving the system of equations described in table 1. In order to isolate a section of the riser,
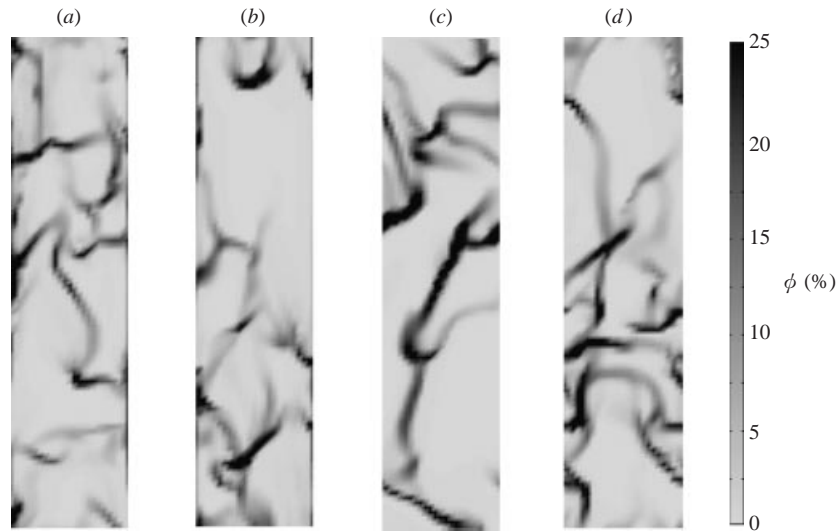
FIGURE 1. Instantaneous greyscale plots of solids volume fraction. 25×100 grids. $Fr_h = 0.0972$; $e_p = 0.9$; $Fr_p = 64.8$; $Re_p = 1.18$; $A = 4$. Average solids volume fraction $= 0.05$. Gas is allowed to slip freely at the walls. Boundary conditions for the particle phase: (*a*) partial slip (specularity coefficient, $\phi' = 0.5$; $e_w = 0.9$); (*b*) free slip; (*c*) doubly periodic domain; (*d*) doubly periodic domain and fixed T. In (*a*) the pressure drop in the gas phase is 99% of the weight of bed, while in (*b*)–(*d*) the pressure drop balances the weight of the bed.

periodic boundary conditions were imposed in the axial (vertical) direction. Two-dimensional simulation results for a domain with an aspect ratio, $A(=\text{height/width})$, of 4 and an average solids volume fraction of 0.05 are presented in figure 1. In dimensionless form, the width of the box, Δ_h, translates to the inverse of a Froude number, $Fr_h = v_t^2/g\Delta_h$. In these simulations, $Fr_h = 0.0972$. (For the combination of parameters in table 1, this translates to a domain width of 5 cm. Note that even though this is a rather small domain when compared to the typical size of risers, the total number of particles is already prohibitively large to track the motion of each and every particle through a Lagrangian simulation. Thus, structures visible in this figure can be examined realistically only through solution of continuum equations of motion.) This figure shows a grey-scale plot of solids volume fraction at one instant of time and for four different wall boundary conditions. In all these simulations, both the solid and gas phases were initially at rest and the volume fraction of solids was uniform at 0.05. Transient integration was then carried out using four different wall boundary conditions and the evolution of non-uniform structure was followed. Figure 1(*a*) shows a snapshot obtained when a partial slip boundary condition proposed by Johnson & Jackson (1987), see table 1, was used for the particle phase, while allowing the gas to slip freely at the wall. Figure 1(*b*) presents a snapshot obtained when both the gas and solid phases were allowed to slip freely at the wall (but not penetrate it). Similar results were obtained with no-slip boundary conditions as well (not shown). It is thus clear that details of the particle–wall interactions are not essential for producing these meso-scale structures.

We then replaced the walls of the channel with periodic boundary conditions (figure 1*c*), so that both the particles and the gas could penetrate the virtual wall and reappear at the other side. Figure 1(*d*) describes a snapshot obtained when only the continuity and momentum balance equations were solved using periodic boundary conditions in both directions, while fixing the value of the granular temperature at the

value corresponding to the uniformly fluidized state and treating it as independent of time and position. While a direct comparison cannot be made between the four parts of figure 1, all of them show the presence of non-uniform strand and cluster-like structures.

These results indicate that, in this class of flow problems, macroscopic shear arising from the presence of boundaries is not required to induce meso-scale structures. Therefore, one should be able to identify the different routes that lead to cluster formation by simply examining the stability of uniform flow of gas–particle mixtures in unbounded domains.

4. Various routes to formation of clusters in gas–particle flows

Although attractive inter-particle forces can give rise to aggregation of fine particles, this is not likely to be a dominant route to cluster formation under the high-velocity, rapid shear flow conditions encountered in typical riser applications. Therefore, it is reasonable to focus our attention on flow-induced inhomogeneities and ask if such structures arise as a result of instabilities that can be recognized by a stability analysis of the averaged equations of motion. To this end we briefly review the stability of several simple, idealized flows.

4.1. *Stability of the uniformly fluidized state*

Returning to equations (1)–(4), consider first the uniformly fluidized state of a gas–particle suspension. This problem has been investigated by a number of researchers who have sought to elucidate the origin of bubbles in *dense* fluidized beds and the distinction between bubbling and non-bubbling systems. A detailed discussion of this stability analysis, including the history, can be found in recent articles by Anderson, Sundaresan & Jackson (1995) and Glasser, Kevrekidis & Sundaresan (1996, 1997). Focusing on gas–particle systems, it can now be asserted that dense fluidized beds are most unstable to vertically travelling wavefronts having no horizontal structure, and that bubbles emerge through a loss of stability of these wavefronts to horizontal perturbations. In these analyses, a simple Newtonian form has been assumed for the particle- and fluid-phase stress tensors, where the particle-phase pressure, p_s, and viscosity, μ_s, were taken to be monotonically increasing functions of the solids volume fraction, ϕ, and the effective viscosity of the gas phase was simply set to be that of the gas itself. The gas was assumed to be incompressible and the gas-phase pressure p_g was found by solving the equations of motion. The drag coefficient was modelled using the Richardson–Zaki equation (Richardson & Zaki 1954).

Glasser, Sundaresan & Kevrekidis (1998) have extended this stability analysis to uniformly fluidized suspensions covering the entire range from dense fluidized beds to dilute systems representative of riser flow. It was found that for every value of particle volume fraction the uniformly fluidized state is most unstable to vertically travelling wavefronts having no horizontal structure. Furthermore, a loss of stability of this vertically travelling wavefront to transverse perturbations gives rise to a travelling wave having a lateral structure in exactly the same manner, irrespective of whether we are considering a dense fluidized bed or a dilute gas–particle suspension. The structure of solutions having both vertical and lateral non-uniformities in the velocity and particle volume fraction fields changes smoothly from a bubble in the case of a dense fluidized bed to a cluster of particles in the case of a dilute suspension. Thus, it has been shown that bubbles in dense beds and clusters in dilute systems emerge through the same instability and that the averaged equations (1)–(4) with simple phenomenological closures can capture the formation of these structures. These

structures arise because of an interaction between inertia associated with the particle phase, gravity and gas–particle drag. Their dominant length scale, L, is given by $L = (\mu_s v_t / \rho_s g)^{1/2}$. Physically, this particular route to cluster formation arises because of the existence of a relative motion between the particles and the gas. Redistribution of a uniform suspension of particles into clusters surrounded by a region containing a comparatively lower concentration of particles creates a path of lower resistance for the particles to fall down under the action of gravity and the gas to rise.

4.2. *Non-uniform structures arising from inelastic collisions*

Clusters form as a result of inelastic collisions both in granular materials under rapid shear and in the cooling of granular gas. Hopkins & Louge (1991) noted in their simulation of plane shear flow of inelastic disks that a non-uniform microstructure could arise when the collisions between the disks are sufficiently inelastic. This work has spawned particle dynamics simulations (e.g. see Goldhirsch, Tan & Zanetti 1993; McNamara & Young 1996; Tan & Goldhirsch 1997) and experiments (e.g. see Kudrolli & Gollub 1997) on clustering due to inelastic collisions.

The extent to which the formation of clusters as a result of inelastic collisions between particles can be captured by continuum equations of motion for the granular material has also been investigated extensively (e.g. see Savage 1992; Tan 1995; McNamara & Young 1996; Tan & Goldhirsch 1997; Nott *et al.* 1999). Collectively, these studies suggest that the kinetic theory of granular materials does reveal the existence of such clustering.

Given that inelastic collisions and inertial instability associated with fluidization can individually give rise to clusters and streamers, it is hardly surprising that these two mechanisms, when acting together, can also lead to such structures. When an interstitial fluid is present, the damping of the fluctuating motion of the particles by this fluid augments the tendency to form clusters (Wylie & Koch 2000).

Several researchers have investigated the dynamics of fluidized beds and circulating fluidized beds, using discrete particle simulation (or the discrete simulation Monte Carlo method) to follow the motion of the particles and an averaged equation of motion for the gas (Ito *et al.* 1998; Hoomans *et al.* 1996; Ouyang & Li 1999; Tanaka, Yonemura & Tsuji 1995; Tanaka *et al.* 1997; Tsuji, Kawaguchi & Tanaka 1993; Tsuji, Tanaka & Yonemura 1998). Structures, such as bubbles and slugs in dense fluidized beds and clusters in dilute systems, form readily in these simulations. Thus, the meso-scale structures seen in our transient integration of a continuum hydrodynamic model are indeed physical entities.

Let us now return to the problem of gas–particle flows in risers and take stock of what one can say with some degree of confidence. High-velocity gas–particle flows in risers do show persistent fluctuations and are accompanied by the presence of clusters and streamers. Figure 1 presented earlier has confirmed the ability of the averaged equations of motion for two-phase flow, coupled with an additional equation for the particle-phase kinetic energy, described in table 1 (henceforth referred to as micro-scale equations), to capture clusters and streamers, and predict persistent fluctuations in velocity and particle concentration fields. It is also clear that these non-uniform structures arise as a result of local instabilities and not because of instabilities associated with the entire circulation loop of CFBs. Furthermore, the presence of tube walls is not required for the formation of these structures (figure 1). Instead, they arise because of (*a*) instability associated with the relative motion between the gas and particle phases and (*b*) dissipation of fluctuating energy of particles by inelastic collisions between particles and viscous damping.

While the micro-scale equations summarized in table 1 are not exact, they do seem to capture qualitatively the known routes to meso-scale structures. It would therefore seem reasonable to expect that the numerical integration of these equations, using a sufficiently fine grid structure, should reveal the flow behaviour at both meso- and macro-scales. The typical length scale of meso-scale structures estimated from a stability analysis of the micro-scale equations is of the order of 10–50 particle diameters. This is consistent with the cluster sizes reported by Horio (1995). Therefore, if we truly wish to resolve these meso-scale structures in a numerical integration of the micro-scale equations, the grid size should be of the order of a few particle diameters. Such a highly resolved simulation is simply impractical and will not be a useful design tool for industrial applications.

One is usually most interested in the macro-scale structures and how changes in process design influence them. At the same time, meso-scale structures cannot be ignored as these have a significant effect on the macro-scale features and structures seen in process units such as riser reactors. Indeed some researchers have found that the pressure drop in a FCC riser could not be predicted by their *coarse-grid* simulations unless an apparent particle size (larger than or equal to the true size), parameterized in terms of a Reynolds number and void fraction, was used in the drag law (O'Brien & Syamlal 1994).

Let us now take a closer look at what is implicitly assumed in every coarse-grid simulation of a riser. In the finite volume method, which is the most commonly used method to solve such equations, the domain of interest is divided into a number of cells and balance equations are written for each cell. In simulations of industrial scale risers, the cells are typically hundreds of particle diameters in each direction.

In coarse-grid simulations being performed today, the dependent variables are assumed to be uniform inside such cells. We know, however, that meso-scale structures can and will form in riser flows (see figure 1) and that they are only a few tens of particle diameters in size, which is much smaller than the typical computational cell size. These structures will not be resolved in the coarse-grid simulation.

It is worthwhile to digress at this point to turbulent flow of an incompressible single-phase fluid where no sub-grid-scale instability is present to induce sub-grid flow structure. The dissipative sub-grid-scale processes convert mechanical energy to thermal energy, and therefore, to sustain the sub-grid structure, kinetic energy associated with macro-scale (i.e. a length scale larger than the grid size) motion must be converted continually to that associated with sub-grid-scale flow. This is possible only when macro-scale shear is present. Indeed, the effective viscosity in large-eddy simulations depends on the grid size and the macro-scale shear rate (e.g. see Ferziger & Peri 1996; Smagorinsky 1963). Returning to the present two-phase flow problem, it is therefore natural to expect the corrections to the effective stresses and the inter-phase interaction force to depend on the macro-scale shear rates in the particle and gas phases. However, the presence of a macro-scale shear is *not* necessary for inducing a sub-grid structure in our problem.

5. Some results on effects of meso-scale structures

The meso-scale structures due to local instabilities can be understood better by performing highly resolved simulations of a small region of a riser. Furthermore, as the presence of boundaries is not necessary to induce the formation of meso-scale structures, one can isolate a region of the riser by simply utilizing periodic boundary conditions in all directions. With this in mind, we performed a number of two- and

three-dimensional simulations† of the equations in table 1 in rectangular domains and invoked periodic boundary conditions in both lateral and vertical directions. (Such statistical properties may also be gathered by particle dynamics simulations.)

In these simulations, the gas pressure varied periodically in the lateral direction, while in the vertical direction it was partitioned into a periodic part and a linear part. The linear part contributed to a mean pressure gradient in the vertical direction whose value was chosen to balance the total gravitational force acting on the suspension. Henceforth, when we say that periodic boundary conditions are imposed in the axial direction, it is implicitly understood that gas pressure is treated in this manner.

Before discussing results gathered from our simulations in periodic domains, it is important to reiterate the connection between these simulations and a coarse-grid CFD simulation of gas–particle flows in a large riser. The coarse-grid simulations do not resolve the meso-scale structures which are smaller than the grid size. Our ultimate goal is to devise a sub-grid model to account for the role of the sub-grid-scale structure. Our present objective is to bring forth the general features of the sub-grid model. The sub-grid structure is dictated by a combination of sub-grid-scale instabilities and macro-scale shear. We focus first on the former and briefly touch upon the latter at a later stage.

We consider below gas–particle flows in periodic domains whose dimensions are comparable to the grid size in typical coarse-grid CFD simulations, and perform as highly resolved simulations (using a second-order discretization scheme, see Syamlal 1998) as we can with our computational resources. From these computations we have gathered statistical data on the effects of meso-scale structures.

We first present in figure 2 an example to demonstrate that as one increases the resolution, finer and finer structures are revealed. The average solids volume fraction in the domain is 0.05. The initial conditions represent a very slight perturbation of the uniform solution afforded by the equations of motion in table 1. Figure 2(*a*) shows a (representative) snapshot of the solid volume fraction field at one particular instant of time obtained in a simulation using 25×10 equally sized grids. As we increased the resolution, meso-scale structure in the form of many thin strands and clusters were observed. Figure 2(*b*) shows a snapshot obtained with 25×100 grids, while that in (*c*) corresponds to 50×200 grids. The simulation in (*a*) clearly smears the fine-scale features seen in (*b*) and (*c*).

5.1. *Effect of meso-scale structure on drag and pseudo-thermal energy production/dissipation*

It is natural to inquire if the meso-scale structure, which may get resolved by fine-grid simulations, really has any bearing on quantities averaged over the domain. To

† Ideally, one should perform only three-dimensional simulations; however, each three-dimensional simulation of the type we would like to carry out requires nearly 100 times more CPU time than a corresponding two-dimensional calculation. As we need to perform many sets of simulations to bring out the fundamental ideas discussed in this paper, three-dimensional simulations are simply beyond our current resources. While the two-dimensional calculations are less satisfactory than the three-dimensional simulations, they suffice to make a convincing case for the need for sub-grid models. It should be noted that two-dimensional simulations are not useful in single-phase calculations, as there is no meaningful equivalent of vortices (eddies) in two-dimensions. In the case of the present two-phase flow problem, the large-wavenumber portion of the energy spectrum is primarily controlled by the local instabilities. As all the known local instabilities in the gas–solid systems are revealed by the equations at the two-dimensional level itself, there is some basis for hoping that two-dimensional simulations can provide an initial glimpse of the sub-grid model.
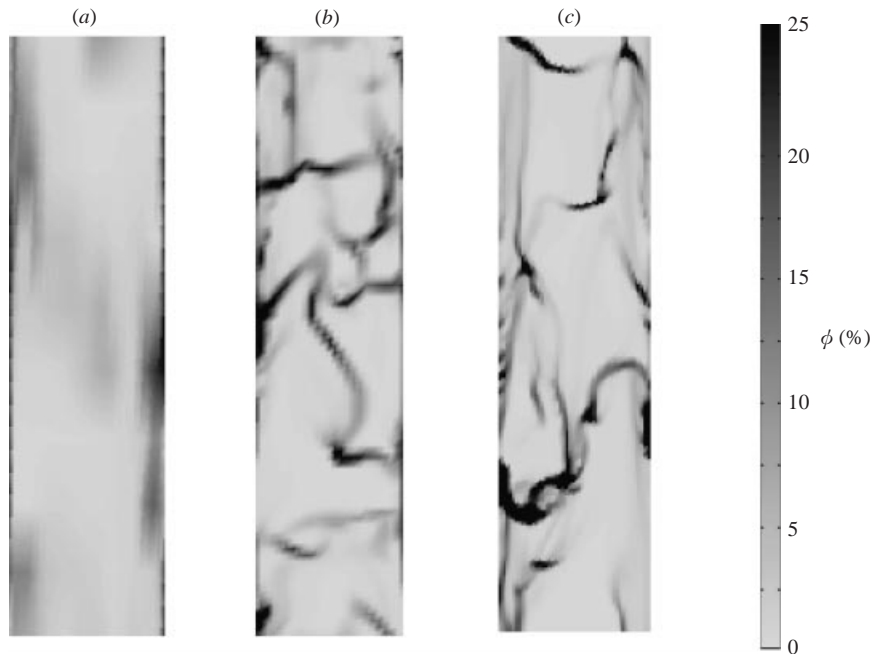
FIGURE 2. Instantaneous greyscale plots of solids volume fraction. $Fr_h = 0.0972$; $e_p = 0.9$; $Fr_p = 64.8$; $Re_p = 1.18$; $A = 4$. Average solids volume fraction $= 0.05$. Number of grids: (*a*) 25×10; (*b*) 25×100; (*c*) 50×200.

address this issue, consider the results of a simulation presented in figure 3. The parameters are the same as in figure 2(*c*). Figure 3(*a*) shows the temporal evolution of the spatially Favre-averaged granular temperature. (Henceforth, we refer to such an average as the *domain-average*.) After an initial induction period (whose duration depends on the initial conditions), the domain-average temperature shows persistent fluctuations. Typical time step in these simulations is 10^{-2} dimensionless units. The average temperature for this fluctuating state is quite different from that in the uniform state (which was the starting value of the temperature in this figure). Such averaging is typically done for a minimum of 50 units of dimensionless time. (Henceforth, we refer to the time-averaged value of any domain-average quantity simply as the *average* value of that quantity.) The corresponding spatially Favre-averaged velocities of the gas and particle phases in the vertical directions were also calculated as functions of time. The difference between these two velocities, i.e. the domain-average slip velocity, is plotted in figure 3(*b*). Again we see that the average slip velocity in the fluctuating state is substantially different from that in the (initial) uniform state. Stated differently, the slip velocity needed to produce a specified amount of drag force is larger in the presence of meso-scale structure when compared to a corresponding uniform structure. It is also important to note that the instantaneous value of the domain-average slip velocity fluctuates appreciably in the statistical steady state, indicating the dynamic nature of the meso-scale structures.

The two panels on the right are the same as those on the left except that the so-called model B, where the gas-phase pressure gradient appears only in the gas-phase momentum balance, was used for the micro-scale equations. The inter-phase interaction term in model B will differ from that of model A by a factor $(1 - \phi)$ (Bouillard, Lyczkowski & Gidaspow 1989), so both models yield identical uniform
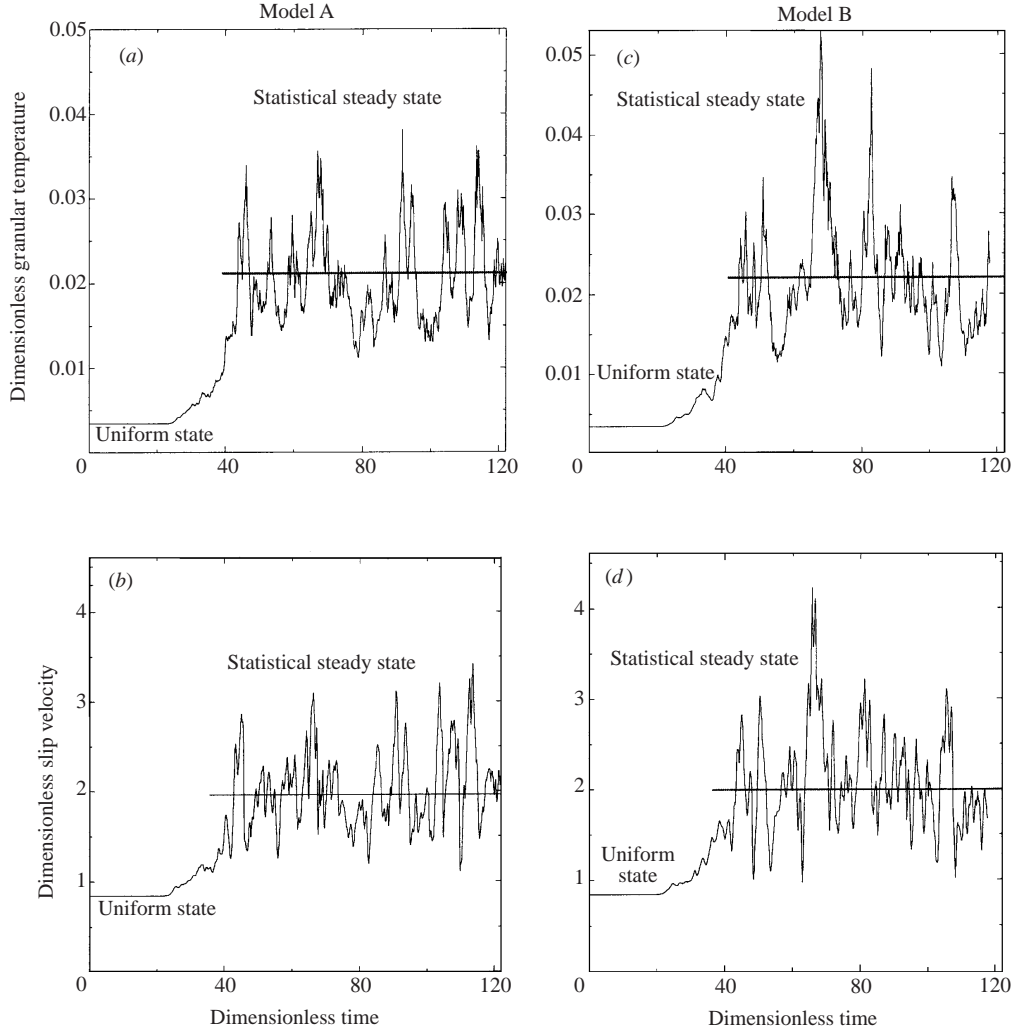
FIGURE 3. Temporal evolution of the Favre-averaged granular temperature and the Favre-averaged axial slip velocity. (a,b) Model A; (c,d) Model B: 50×200 grids. $Fr_h = 0.0972$; $e_p = 0.9$; $Fr_p = 64.8$; $Re_p = 1.18$; $A = 4$. Average solids volume fraction $= 0.05$.

state solutions. In the absence of viscous terms, model A is ill-posed, while model B is not. It is clear from figure 3 that both models A and B predict persistent fluctuations. Indeed the average granular temperature and the slip velocity are almost the same in the two cases.

Figure 4 illustrates the effect of grid resolution on the average slip velocity, W_{slip}, and the average granular temperature. As the grid size is decreased, the meso-scale structures are better resolved, resulting in appreciable changes in the slip velocity and average granular temperature. Both the average granular temperature and W_{slip} become roughly independent of grid resolution, as the meso-scale structures become better and better resolved. The small grid-size dependence seen in figure 4 at the three smallest grid sizes is much smaller than the standard deviation of the temporal fluctuations (e.g. see figure 3). Examination of the power spectra of the variable fields also indicates convergence: as the resolution is increased the power spectra at the
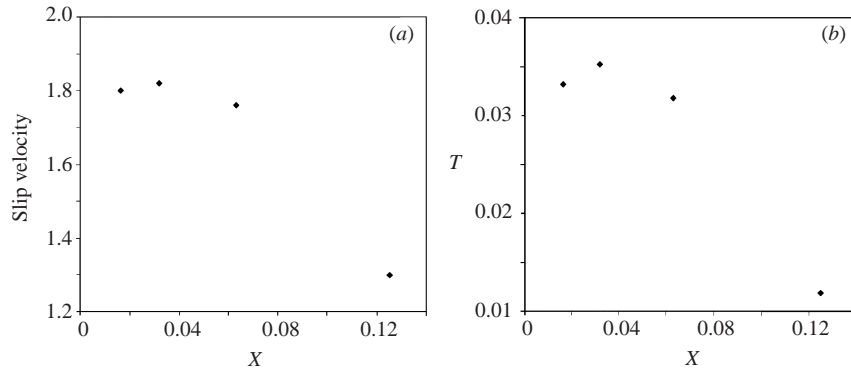
FIGURE 4. Effect of resolution on domain-averaged quantities. $Fr_h = 0.486$; $e_p = 0.9$; $Fr_p = 64.8$; $Re_p = 1.18$; $A = 1$. Average solids volume fraction $= 0.05$. (*a*) Dimensionless slip velocity; (*b*) dimensionless granular temperature. X denotes $1/N$, where N is the number of grid points in each direction. $X = 1$ corresponds to uniform state, where $W_{slip} = 0.85$ and $T = 0.0034$.
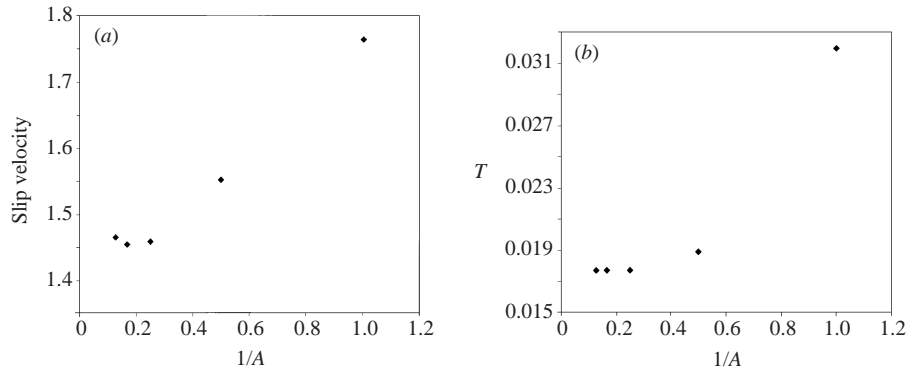

FIGURE 5. Effect of aspect ratio on domain-averaged quantities. $Fr_h = 0.486$; $e_p = 0.9$; $Fr_p = 64.8$. $Re_p = 1.18$. Average solids volume fraction $= 0.05$. (*a*) Dimensionless slip velocity; (*b*) dimensionless granular temperature. Resolution: $(16 \times 16A)$ grids. At the uniform state, $W_{slip} = 0.85$ and $T = 0.0034$.

lower wavenumbers do not change (Agrawal 2000). It can therefore be said with confidence that meso-scale structures begin to appear at modest grid resolution, and they persist as we continue to increase the grid resolution. Thus, the effects of the meso-scale structures seen in our simulations are not numerical artifacts.

Figure 5(*a, b*) shows that the average temperature and slip velocity decrease upon increasing the aspect ratio, and become essentially independent of A for $A \gtrsim 4$. Snapshots of particle volume fraction field, presented in figure 6, clearly show that the meso-scale structures obtained at different aspect ratios are very similar.

We have carried out two-dimensional simulations such as the one shown in figures 3–5 (using model A) for several different combinations of parameters. After each simulation has been run for a long enough duration to ensure that a statistical steady state has been reached (typically at least 50 units of dimensionless time), statistics on a variety of fluctuating quantities have been obtained. The effect of e_p on various domain-averaged quantities is illustrated in table 3. This table presents the magnitude of each quantity at the uniformly fluidized state and its average value obtained from transient simulations in a periodic domain with an aspect ratio of 4 and $Fr_h = 0.486$

	Uniform state					Statistically steady state				
e_p	0.8	0.9	0.9*	0.9**	0.99	0.8	0.9	0.9*	0.9**	0.99
W_{slip}	0.85	0.85	0.85	0.85	0.85	1.60	1.46	1.49	1.68	1.27
T	0.0032	0.0034	—	.0041	.0036	0.015	0.018	0.016	0.017	0.025
$J_{coll}(\times10^{-4})$	1.11	0.63	—	.83	0.07	73.58	52.78	50.71	59.14	8.5
$J_{vis}(\times10^{-4})$	5.5	5.77	—	10.29	6.14	32.36	39.16	35.54	85.6	52.2
$\Gamma_{shear}(\times10^{-4})$	0	0	—	0	0	101.7	88.27	86.25	129.18	57.33
$\Gamma_{slip}(\times10^{-4})$	6.4	6.58	—	11.12	6.21	4.21	3.68	—	15.56	3.41
$P_{s,KT}$	0.0002	0.00023	—	0.00026	0.00024	0.0019	0.0022	0.0021	0.0024	0.0029
$P_{s,meso,x}$	—	—	—	—	—	0.028	0.032	0.031	0.032	0.020
$P_{s,meso,y}$	—	—	—	—	—	0.018	0.015	0.016	0.025	0.012

TABLE 3. Effect of coefficient of restitution on dimensionless domain-averaged quantities obtained from two-dimensional simulations. $Fr_h = 0.486$; $Fr_p = 64.8$; $Re_p = 1.18$; $A = 4$. Average solids volume fraction $= 0.05$. Here, subscripts x and y denote the horizontal and vertical directions, respectively. Resolution: 16×64.
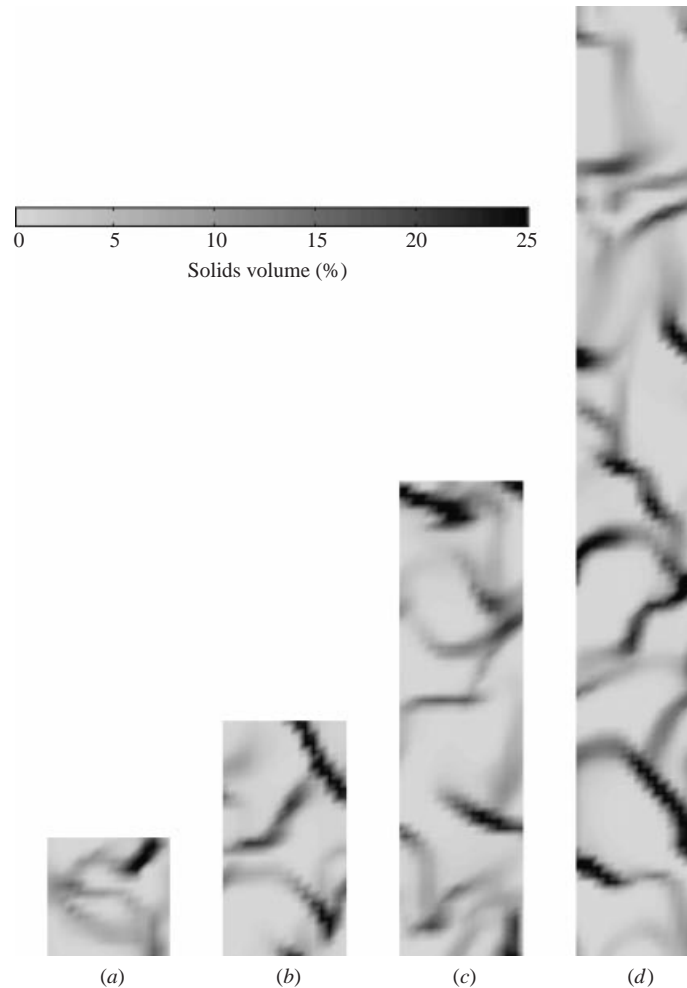
FIGURE 6. Instantaneous greyscale plots of solids volume fraction, revealing meso-scale structures. $Fr_h = 0.486$; $e_p = 0.9$; $Fr_p = 64.8$; $Re_p = 1.18$; (a) $A = 1$; (b) $A = 2$; (c) $A = 4$; (d) $A = 8$. Resolution: $(16 \times 16A)$ grids.

using 16×64 grids. According to the model, the slip velocity in the uniform state is independent of e_p, while this is not the case in the statistical steady state. Furthermore, the granular temperature in the statistical steady state is appreciably larger than that in the uniform state in the entire range of e_p values shown in table 3. It should be noted that the closure relations for the stresses, conductivity of PTE and the rate of dissipation due to inelastic collisions derived by Lun *et al.* (1984) are valid for only slightly inelastic collisions. We have explored a somewhat wider range of e_p values in table 3 to demonstrate that the effect of e_p on the average quantities is only gradual.

It is also interesting to discuss at this stage the relative importance of the different routes for production and dissipation of PTE. Let us first consider the production of PTE due to gas–particle slip (see (16) in table 1). In the absence of this term, the PTE of the particles in a uniformly fluidized suspension is zero. Thus, this term gives the particle phase in a uniformly fluidized suspension a small, but non-zero, PTE, which, in turn, imparts the particle phase with a non-zero pressure and viscosity. Once the
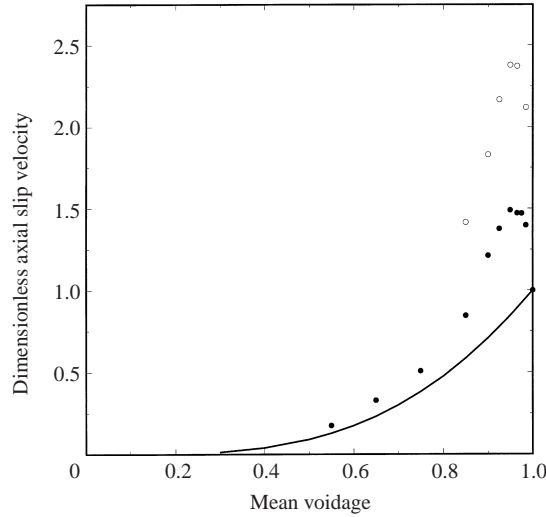
FIGURE 7. Variation of effective slip velocity with voidage. Both are domain-averaged quantities. $e_p = 0.9$; $Fr_p = 64.8$; $Re_p = 1.18$. ●, $Fr_h = 0.486$; $A = 4$; resolution: 16×64. ○, $Fr_h = 0.243$; $A = 2$; resolution: 32×64. Solid line: uniform state.

uniform state of the mixture has given way to a non-uniform distribution consisting of meso-scale structures, production of PTE occurs predominantly through shear (see rows labelled Γ_{shear} and Γ_{slip} in table 3).

In one simulation, with $e_p = 0.9$, the slip-production of PTE was turned off after the system developed a non-uniform structure and the simulation was continued for a sufficiently long period of time to gather statistics. The results obtained in this numerical experiment are shown in table 3 as a separate column (labelled 9*). Also show in this table are the results obtained in another numerical experiment (also at $e_p = 0.9$) where the full expressions for Γ_{slip} and J_{vis} proposed by Koch & Sangani (1999), described earlier in (19)–(21) were used (see column labelled 9**). A comparison of the entries in the three columns labelled $e_p = 0.9$ reveals clearly that slip is of secondary importance in the system being simulated.

Table 3 also summarizes the statistical average values of the rates of PTE dissipation by gas–particle slip and by inelastic collisions. In the uniform state and $\phi = 0.05$, $J_{vis} \gg J_{coll}$. In contrast, both routes are equally important in the statistical steady state. It is intuitively obvious that as the loading level decreases, the viscous damping will become increasingly more important, and vice versa. It can also be seen from this table that the average rate of dissipation in a state of non-uniform microstructure is actually larger than that in the corresponding uniform state. Thus, a higher average granular temperature is sustained in the non-uniform state through enhanced rate of production of PTE by shear and not because of a lowering of the rate of dissipation. Comparing the statistical steady states shown in the three columns labelled 9, 9* and 9**, we see that the expression derived recently by Koch & Sangani (1999) predicts a considerably larger J_{vis} than the simpler expression we used in the bulk of our simulations. Simultaneously, W_{slip} is also larger, possibly due to larger clusters and streamers, which, in turn, causes larger magnitudes of velocity gradients and larger Γ_{slip}.

Let us now return to the question of what is needed to properly simulate gas–particle flows in large vessels. It is clear from the examples described above that coarse-grid simulations which completely ignore the sub-grid microstructure will overestimate the

drag force and underestimate the rates of production and dissipation of PTE. A rather simple correction for the drag force term may be determined as follows. Suppose we wish to simulate gas–particle flow in a large process unit using grids of a particular size. Taking this grid size to be used in the coarse-grid simulation of the large unit as the *domain size*, and imposing periodic boundary conditions in all directions, one can carry out simulations of the type described above for various mean volume fractions. The average values of the slip velocity at various particle loading levels may then be used to extract an approximate drag law. This is illustrated in figure 7, where the statistical average slip velocities obtained in simulations carried out over a doubly periodic domain with $Fr_h = 0.486$ and $A = 4$ are shown by filled circles. These data can be captured satisfactorily by some expression of the form $\langle v \rangle / v_t = F_1(\phi)$, where v_t is the terminal velocity of a single particle. A plausible functional representation of the apparent drag, which directly utilizes $F_1(\phi)$, is given in Appendix A. (It should, however, be noted that a proper representation of the effective interaction force between the gas and particle phases, which must be used in coarse-grid simulations, should include both mean and fluctuating components. This may necessitate the use of a stochastic model. See Appendix A for further details.)

The variation of the apparent slip velocity as a function of voidage (shown in figure 7 by filled circles) is quite different from that for the uniform state (the solid line in figure 7). The apparent slip velocity first increases as the voidage decreases. This is a result of the formation of denser clusters for higher mean solids volume fraction (see figure 8a, b). The denser clusters fall faster relative to the surroundings. Gas bypassing the clusters is clearly evident in figure 9. But as the voidage is decreased further, the clusters start interacting and intersecting one another, making it more difficult for the gas to bypass the dense regions (see figure 8d). As a result, the slip velocity starts decreasing with decreasing voidage. At a certain voidage there is a transition from the formation of clusters to the formation of voids (see figure 8e). For lower voidages still, the system forms voids, or bubbles, instead of clusters (see figure 8f). It should be emphasized at this stage that the apparent slip velocity for a specified mean solids fraction is dependent on grid size to be used in the coarse-grid simulations. To highlight this point, we have also included in figure 7 the apparent slip velocities obtained for some simulations in a doubly periodic domain that is twice as wide (open circles in figure 7). The domain height is the same for both cases. The apparent slip velocities in this case are larger than those for the narrower domain; the trend, however, is similar.

As the size of the domain decreases, the apparent slip velocity decreases towards the value corresponding to a uniform state (equivalently, the apparent particle size decreases toward the true particle size). Needless to say, the *sub-grid* model for apparent drag obtained in this manner by simply averaging over the domain is crude and closer scrutiny of the details of the meso-scale structure is needed for more fundamental sub-grid models. It should be emphasized, however, that even the crude sub-grid model sketched above for the apparent drag is a rational improvement over an utter disregard of the meso-scale structure.

We performed a limited number of three-dimensional simulations in periodic domains to demonstrate that the meso-scale structures and their effects are not artifacts of two-dimensional simulations. Figure 10 shows a vector plot of gas velocity, superimposed on a three-dimensional density plot of solids volume fraction field. The tendency of the gas to bypass the dense regions is clearly evident. Figure 11 shows surface plots of solids volume fraction, revealing a gradual transition from clusters to bubbles as the mean solids volume fraction increases.
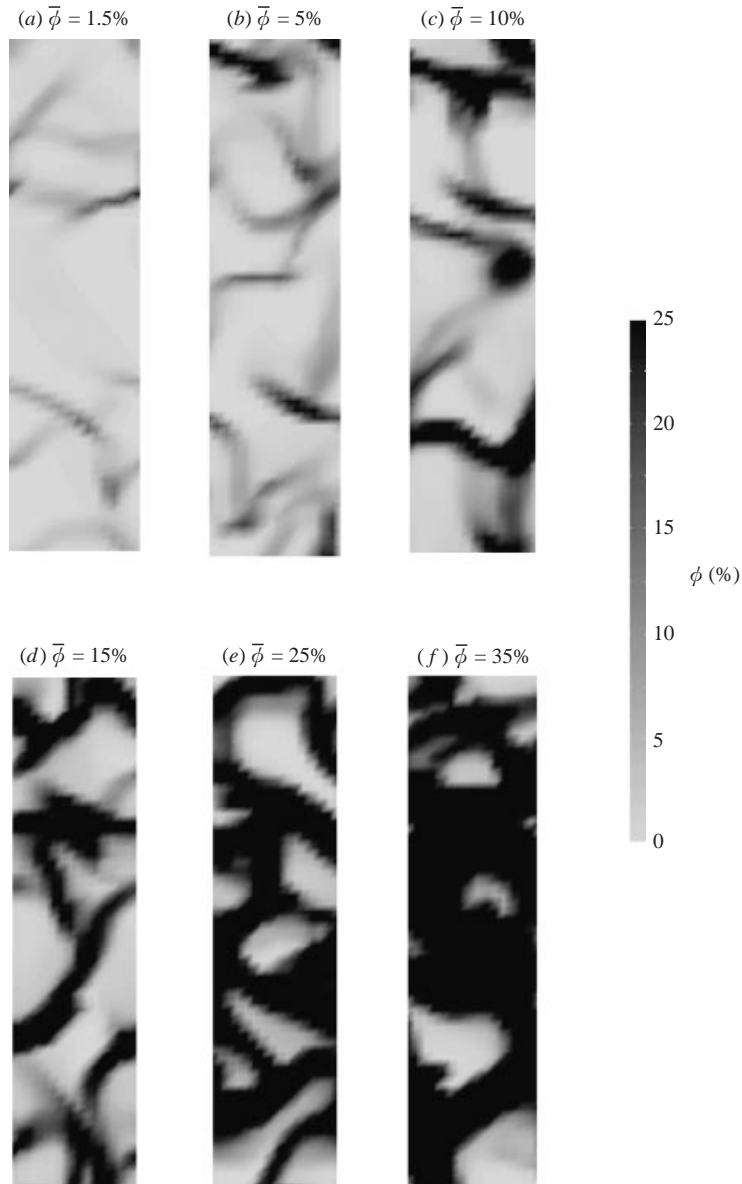
FIGURE 8. Instantaneous greyscale plots of solids volume fraction at various mean solids volume fraction levels. $e_p = 0.9$; $Fr_p = 64.8$; $Re_p = 1.18$; $Fr_h = 0.486$; $A = 4$. Resolution: 16×64.

A comparison of the average axial slip velocities at various values of mean voidages obtained in two-dimensional and three-dimensional simulations at a comparable resolution is presented in figure 12. It is abundantly clear that the effect seen in two-dimensional simulations earlier (figure 7) is present in three-dimensional as well. It is easier for the gas to bypass clusters in three than in two dimensions, making the effect more pronounced in the former. In spite of the quantitative differences, it is apparent that two-dimensional simulations do capture the effect of meso-scale structures qualitatively.
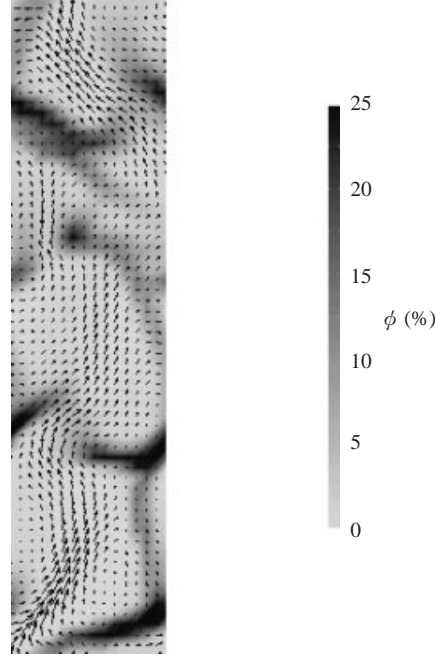
FIGURE 9. Gas bypassing clusters and strands. Snapshot at one instant of time. Vector plot of gas velocity field is superimposed on greyscale plot of solids volume fraction. $e_p = 0.9$; $Fr_p = 64.8$; $Re_p = 1.18$; $Fr_h = 0.486$; $A = 4$. Resolution: 16×64. Average solids volume fraction = 0.05.

5.2. *Role of meso-scale structure on effective stresses*

The effective gas- and particle-phase stresses in coarse-grid simulation of gas–particle flows in large vessels should include the micro-scale stresses (appearing in equations (3) and (4) in table 1) and those due to the sub-grid-scale structures. In large-eddy simulation of single-phase turbulent flow, the latter usually dominates the former. We will now illustrate that this is indeed the case in our problem as well.

Dimensionless meso-scale normal stresses, $P_{s,meso,x}$ and $P_{s,meso,y}$, and microscale pressure, $P_{s,kt}$, in two-dimensional simulations were computed as follows. The domain-averaged values of $\boldsymbol{\sigma}_s$ and $\phi \boldsymbol{v}\boldsymbol{v}$ were first computed as functions of time. These were then time-averaged to obtain $\langle \boldsymbol{\sigma}_s \rangle$ and $\langle \phi \boldsymbol{v}\boldsymbol{v} \rangle$, respectively. Finally,

$$P_{s,meso,x} = \langle \phi v_x v_x \rangle - \bar{\phi}\tilde{v}_x\tilde{v}_x + \langle \sigma_{s,xx} \rangle, \quad P_{s,meso,y} = \langle \phi v_y v_y \rangle - \bar{\phi}\tilde{v}_y\tilde{v}_y + \langle \sigma_{s,yy} \rangle,$$

where $\bar{\phi}$ is the average solids volume fraction in the domain and $\tilde{\boldsymbol{v}}$ is the Favre-average velocity of the particle phase with respect to the mass-average velocity of the mixture (the averaging being done over both space and time). The values of $P_{s,kt}$ (defined as $(1/3)\,\mathrm{tr}\langle \boldsymbol{\sigma}_s \rangle$), $P_{s,meso,x}$ and $P_{s,meso,y}$ for a representative set of simulations are shown in table 3. The generation of PTE by shear associated with meso-scale structures increases the value of $P_{s,kt}$ by an order of magnitude over the value at the uniform state. $P_{s,meso,x}$ and $P_{s,meso,y}$ are even larger, showing that fluctuations associated with the meso-scale structures contribute significantly to the effective normal stresses in coarse-grid simulations.

Figure 13(a,b) summarizes $P_{s,meso,x}$, $P_{s,meso,y}$ and $P_{s,kt}$ values obtained for several different values of $\bar{\phi}$, corresponding to the conditions shown by filled circles in figure 12. At every value of $\bar{\phi}$ shown in figure 13(a,b), $P_{s,meso,x}$ and $P_{s,meso,y}$ are
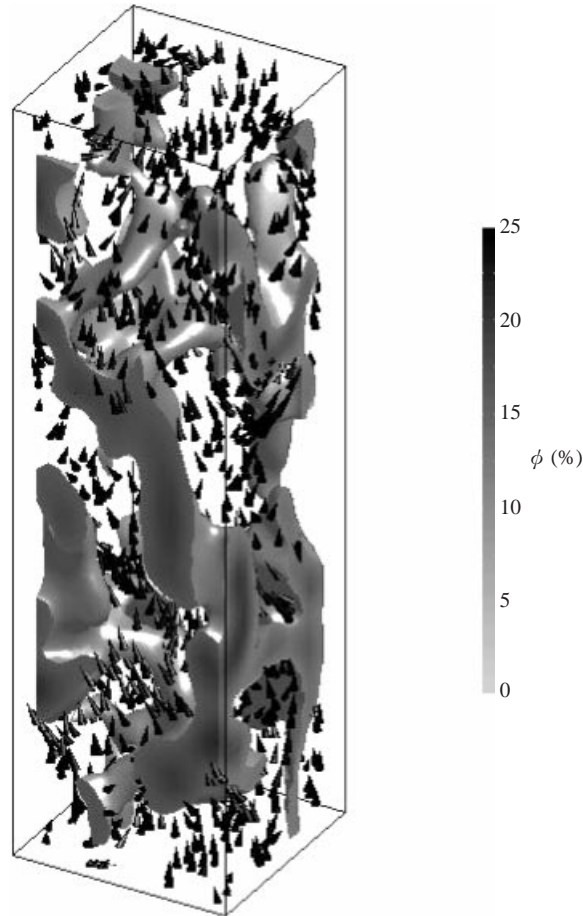
FIGURE 10. Snapshot of solids volume fraction and gas velocity fields in a three-dimensional simulation. Cones represent gas velocity, with orientation and length indicating direction and magnitude, respectively. A contour plot of surface in the interior of the domain where $\phi = 0.05$ is shown. The solids volume fraction at points on the faces is as in the greyscale (provided ϕ here exceeds 0.05). Mean solids volume fraction = 0.05. $e_p = 0.9$; $Fr_p = 64.8$; $Re_p = 1.18$; $Fr_h = 0.486$. Resolution: $16 \times 16 \times 64$. Aspect ratio of the box $1:1:4$.

significantly larger than $P_{s,kt}$ (which, in turn, is much larger than $P_{s,kt}$ corresponding to the uniform state).

The values of horizontal and vertical meso-scale stresses and $P_{s,kt}$ obtained in three-dimensional simulations at various values of $\bar{\phi}$, corresponding to the conditions presented earlier by open circles in figure 12, are shown in figure 14(a,b). The horizontal normal stress in three dimensions is noticeably smaller than that in two dimensions, while $P_{s,kt}$ (three-dimensional) is larger than that in two dimensions. Recall that, in our simulations, the shear due to the meso-scale structures produced PTE and gave rise to $P_{s,kt}$. If the meso-scale structures were not resolved in the simulations, the value of $P_{s,kt}$ would have been much smaller (see columns marked 'uniform state' in table 2). Therefore, it can be concluded that coarse-grid simulations, which do not account for the particle-phase pressure due to the sub-grid-scale clusters and streamers, are grossly inaccurate.

The contribution of the meso-scale structure to the effective gas-phase pressure is

(a) $\bar{\phi} = 2.5\%$ (b) $\bar{\phi} = 5\%$ (c) $\bar{\phi} = 10\%$ (d) $\bar{\phi} = 15\%$

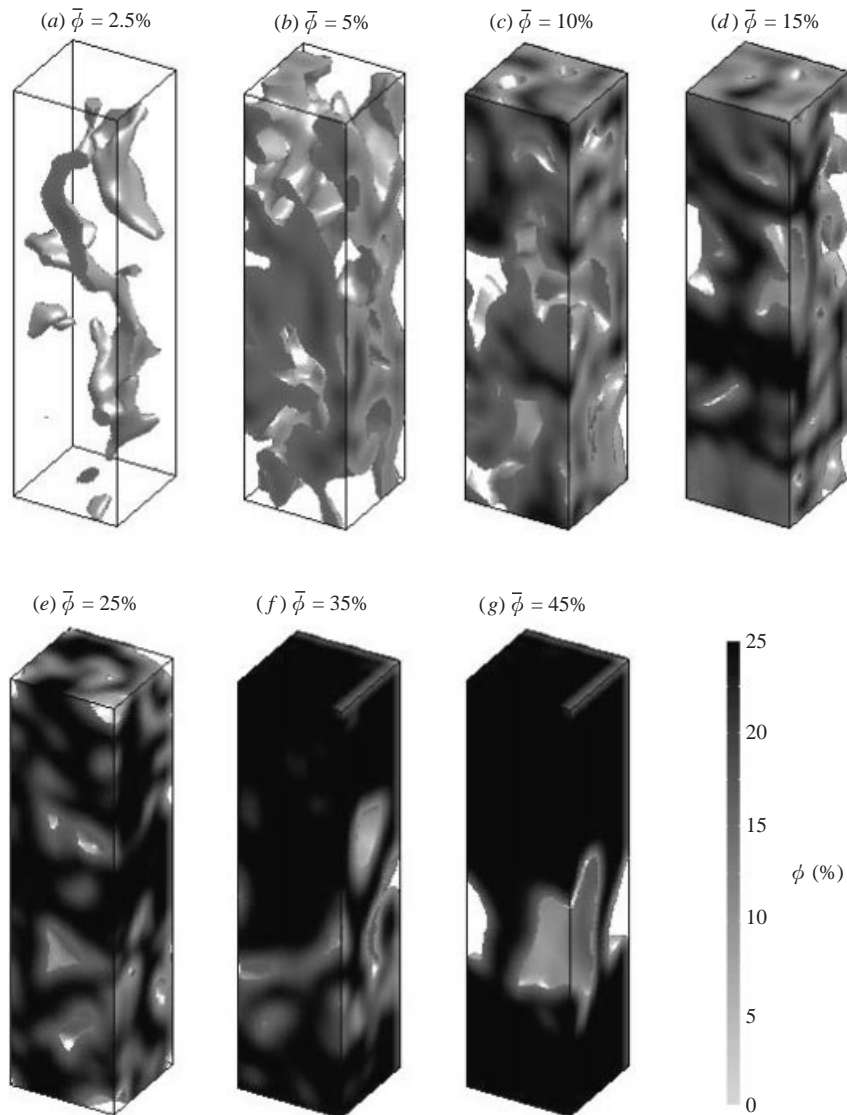(e) $\bar{\phi} = 25\%$ (f) $\bar{\phi} = 35\%$ (g) $\bar{\phi} = 45\%$

FIGURE 11. Snapshots of solids volume fraction fields in a three-dimensional simulation. A contour plot of surface in the interior of the domain where $\phi = 0.05$ is shown. The solids volume fraction at points on the faces is as in the greyscale (provided ϕ here exceeds 0.05). $e_p = 0.9$; $Fr_p = 64.8$; $Re_p = 1.18$; $Fr_h = 0.486$. Resolution: $16 \times 16 \times 64$. Aspect ratio of the box $1 : 1 : 4$.

not included in table 2. As we have treated the gas phase as incompressible, the gas pressure is solved to satisfy incompressibility and the meso-scale contribution to the pressure ($P_{g,meso}$) can simply be absorbed into the pressure term. Strictly speaking, this term needs to be included in the effective pressure in the gas phase in compressible flow problems.

Table 4 presents an illustration of the sensitivity of the values of various average quantities to the choice of model for the effective viscosity of the gas phase. In all the simulations discussed thus far, the effective viscosity of the gas phase was simply taken to be that of the gas itself, and the results obtained with this choice
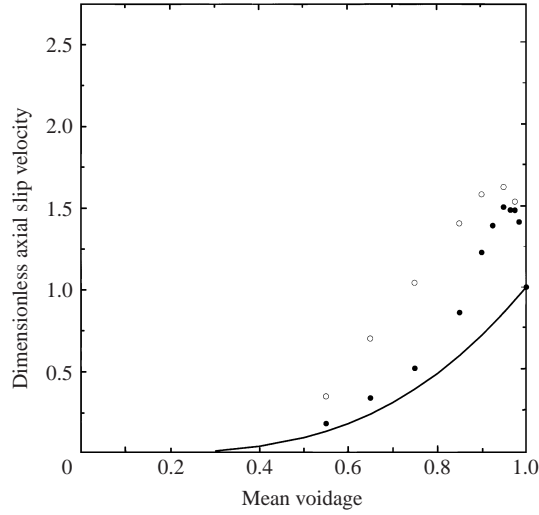
FIGURE 12. Variation of effective slip velocity with voidage. Both are domain-averaged quantities. $e_p = 0.9$, $Fr_h = 0.486$. ●, two-dimensional; aspect ratio $1:4$; resolution: 16×64. ○, three-dimensional; aspect ratio $1:1:4$; resolution: $16 \times 16 \times 64$. Solid line: uniform state.
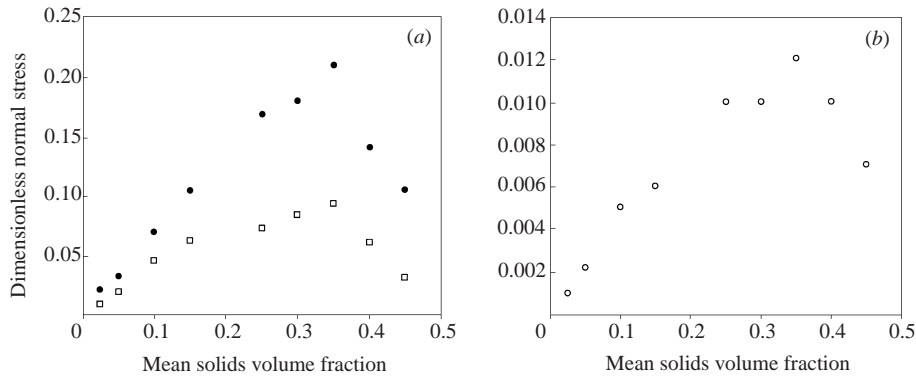

FIGURE 13. Variation of two-dimensional (*a*) meso-scale normal stresses $P_{s,meso,x}$ (●) and $P_{s,meso,y}$ (□), and (*b*) $P_{s,kt}$ (○) with average solids fraction. $e_p = 0.9$; $Fr_p = 64.8$; $Re_p = 1.18$; $Fr_h = 0.486$. Aspect ratio $1:4$. Resolution: 16×64. Here, subscripts x and y denote horizontal and vertical directions, respectively.

are shown as the first column of numbers in this table. The next column employs a standard Smagorinsky (1963) model for viscosity. It is clear from a comparison of these two columns that the average quantities shown there are hardly sensitive to the value of $\hat{\mu}_g$. The final column of numbers was obtained by arbitrarily increasing the Smagorinsky viscosity by a factor of ten, where a small, but detectable, effect of the effective gas-phase viscosity is apparent.

In addition to generating a meso-scale pressure, the meso-scale structures also serve to generate additional deviatoric stresses in the two phases when macro-scale shear is present. We have carried out two-dimensional and three-dimensional simulations in periodic domains, while allowing for the presence of macro-scale shear. In gas–solid flows in vertical risers, axial variation of lateral velocity is present only in a transient fashion but not in a time-averaged sense, whereas lateral variation of axial velocity

	$\hat{\mu}_g = \mu_g$	$\hat{\mu}_g = \mu_g + \mu_{g,t}$	$\hat{\mu}_g = \mu_g + \mu_{g,t}$
W_{slip}	1.46	1.48	1.52
T	0.018	0.018	0.018
$P_{s,KT}$	0.0022	0.0023	0.0024
$P_{s,meso,x}$	0.032	0.033	0.030
$P_{s,meso,y}$	0.015	0.016	0.018

TABLE 4. Dependence of various domain-averaged quantities on the effective viscosity for the gas phase. $Fr_h = 0.486$; $e_p = 0.9$; $Fr_p = 64.8$; $Re_p = 1.18$; $A = 4$. Average solids volume fraction = 0.05. Simulations were carried out in two-dimensional periodic domains. Here, subscripts x and y denote the horizontal and vertical directions, respectively. Resolution: 16×64. In the second and third columns of numbers, gas-phase viscosity (dimensional quantity) is given by $\mu_{g,t} = \rho_g (C\Delta)^2 (\mathbf{S}_g : \mathbf{S}_g)^{1/2}$.
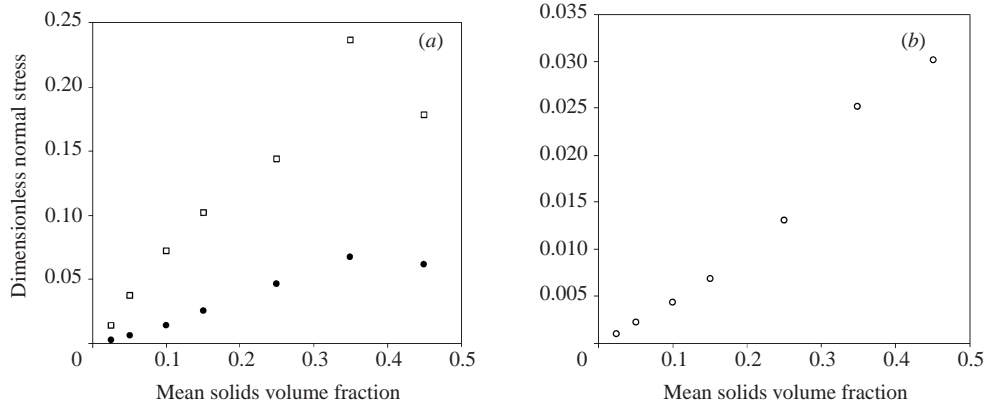

FIGURE 14. Variation of three-dimensional (*a*) meso-scale normal stresses $P_{s,meso,x,z}$ (●) and $P_{s,meso,y}$ (□), and (*b*) $P_{s,kt}$ (○) with average solids fraction. $e_p = 0.9$; $Fr_p = 64.8$; $Re_p = 1.18$; $Fr_h = 0.486$. Aspect ratio $1:1:4$. Resolution: $16 \times 16 \times 64$. Here, subscripts x and z denote horizontal and vertical directions, respectively, while y denotes the vertical direction. $P_{s,meso,x} = P_{s,meso,z} \equiv P_{s,meso,x,z}$.

exists even in a time-averaged sense. This consideration prompted us to focus for the time being only on macroscopic shear in the form of lateral variation of axial velocities of the gas and solid phases.

A schematic of such a simulation in two dimensions is shown in figure 15. From such simulations, we determined $\langle \boldsymbol{\sigma}_s \rangle$, and $\langle \phi \boldsymbol{vv} \rangle$, which were then used to compute $P_{s,meso,x}$, $P_{s,meso,y}$, $P_{s,kt}$ μ_{kt} and μ_{meso}. Here,

$$\mu_{s,kt} = -\frac{1}{\tilde{\gamma}} \langle \sigma_{s,yx} \rangle, \quad \mu_{s,meso} = -\frac{1}{\tilde{\gamma}} \langle \phi v_x v_y \rangle + \mu_{s,kt}.$$

Both $\mu_{s,kt}$ and $\mu_{s,meso}$ are dimensionless quantities, where corresponding dimensional quantities have been scaled in terms of a characteristic viscosity, $\rho_s v_t^3 / g$. $\tilde{\gamma}$ denotes a dimensionless shear rate ($= \gamma v_t / g$ where γ is the shear rate). In general, these viscosities were difficult to compute accurately, requiring long periods of integration (typically over 100 units of dimensionless time). This difficulty stemmed from the large temporal fluctuations of the domain-averaged meso-scale deviatoric stress.

Figure 16(*a–d*) shows the effect of $\tilde{\gamma}$ on W_{slip}, T, $P_{s,kt}$ and μ_{kt}, for three different values of $\bar{\phi}$. Here, μ_{kt} is defined as the average value of kinetic theory viscosity. This is, in general, different from $\mu_{s,kt}$. However, μ_{kt} and $\mu_{s,kt}$ were found to be within a

FIGURE 15. Schematic representation of two-dimensional simulations in periodic domains with imposed shear.

factor of two in our exploratory simulations. For example, at $\phi = 0.05$, $\tilde{\gamma} = 1.113$ and all other parameters as in figure 16, $\mu_{kt} = 1.96 \times 10^{-4}$ and $\mu_{s,kt} = 1.0 \times 10^{-4}$. Therefore, we simply report in figure 16(d) only μ_{kt} (which could be evaluated more accurately). At low shear rates, all four quantities increase modestly with $\tilde{\gamma}$. The fact that these quantities change only modestly with shear rate clearly illustrates that the meso-scale structures arose in these simulations because of inherent instabilities, and were modified by the imposed macro-scale shear. Figure 17(a, b) shows the dependence of $P_{s,meso,x}$ and $P_{s,meso,y}$ on the dimensionless shear rate. The former decreases with $\tilde{\gamma}$, while the latter increases with $\tilde{\gamma}$.

Figure 17(c) shows the effect of $\tilde{\gamma}$ on $\mu_{s,meso}$. It is clear from figures 16(d) and 17(c) that $\mu_{s,meso}$ is larger than μ_{kt} by more than an order of magnitude. Thus, the meso-scale fluctuations cause the system to be more 'viscous' on the macro-scale. It can be shown readily from the equations in table 1 that μ_{kt} of a gas–particle mixture with uniform ϕ increases with shear rate (i.e. shear thickening). When this uniform system gives way to a non-uniform time-dependent structure, the apparent viscosity, $\mu_{s,meso}$, becomes scale-dependent (i.e. dependent on Fr_h and A) and for the combination of Fr_h and A corresponding to figures 16 and 17, it overwhelms μ_{kt}. There is also a qualitative change, namely that at the meso-scale the system now shows a shear-thinning behaviour.

Qualitatively similar behavior is obtained in three-dimensional simulations as well. This is illustrated by the results presented in figure 17(a–c) as filled triangles. Our finding that the meso-scale normal stresses and viscosity overwhelm the corresponding quantities at the particle level clearly shows that the dynamics of the meso-scale structures (characterized by the cluster velocity variance and the associated correlation time) is most relevant for estimating the effective rheological quantities.

The above discussion on the meso-scale stresses clearly suggests that coarse-grid simulations that do not recognize the rather large apparent normal stress and viscosity of the particle phase resulting from sub-grid-scale structure are grossly inaccurate.
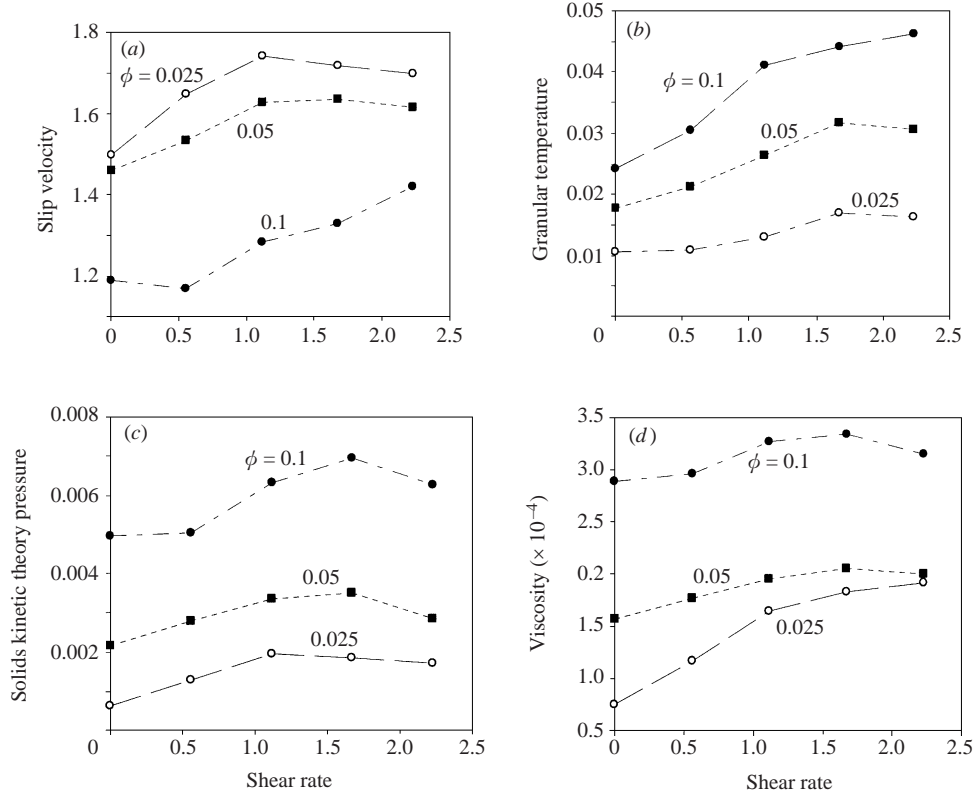
FIGURE 16. Effect of shear rate on (a) W_{slip}, (b) T, (c) $P_{s,kt}$ and (d) μ_{kt}, for three different values of $\bar{\phi}$. $e_p = 0.9$; $Fr_p = 64.8$; $Re_p = 1.18$; $Fr_h = 0.486$. Aspect ratio $1 : 4$. Resolution: 16×64. $\bigcirc$, $\bar{\phi} = 0.025$; $\blacksquare$, $\bar{\phi} = 0.05$; $\bullet$, $\bar{\phi} = 0.10$.

One can readily anticipate that the apparent (meso-scale) viscosity of the gas phase will also be significantly larger than the viscosity used in the detailed simulations. Our efforts to estimate the apparent viscosity of the gas phase due to meso-scale structures, $\mu_{app,g}$, were often unsuccessful because of large (temporal) fluctuation in the domain-averaged value of the $(1 - \phi)u_x u_y$. In any case, there is no doubt that in all our simulations, $\mu_{app,g}$ is much smaller than $\mu_{s,meso}$.

The observed effects of shear rate on meso-scale normal stresses and viscosity are easy to rationalize. At low shear rates the streamers are oriented in a more random fashion and they swing sideways more readily. As the shear rate is increased, they exhibit an increased tendency to orient themselves in the vertical direction.

We performed a limited number of two-dimensional simulations to explore how the average quantities are affected by various dimensionless groups appearing in the model equations.

The dimensionless particle size $(1/Fr_p)$ enters the model in several places:

(i) In the class of flow problems studied here, the local dimensionless slip velocity is typically $O(1)$. Hence, the importance of Fr_p on the drag term can be assessed by considering a situation where the local slip velocity is close to the terminal velocity. In the limit of Stokes drag $(Re_g \ll 1)$ and when $Re_g > 1000$, Fr_p does not appear in the interphase drag term in the dimensionless equations of motion. In these limits,
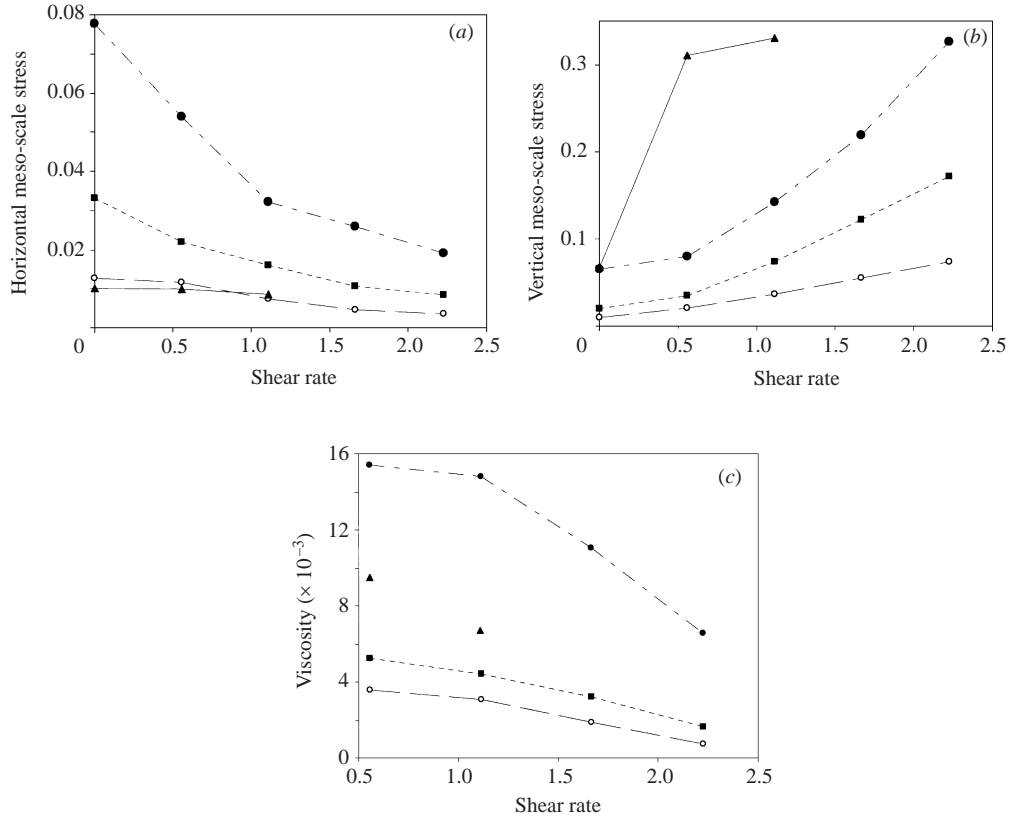
FIGURE 17. Effect of shear rate on the meso-scale normal stresses and viscosity. $e_p = 0.9$; $Fr_p = 64.8$; $Re_p = 1.18$; $Fr_h = 0.486$: ○, two-dimensional; aspect ratio 1:4; resolution: 16×64. $\bar{\phi} = 0.025$; ■, two-dimensional; aspect ratio 1:4; resolution: 16×64. $\bar{\phi} = 0.05$; ●, two-dimensional; aspect ratio 1:4; resolution: 16×64. $\bar{\phi} = 0.10$; ▲, three-dimensional with aspect ratio 1:1:4; resolution: $16 \times 16 \times 64$. $\bar{\phi} = 0.10$. (*a*) Horizontal meso-scale normal stress, $P_{s,meso,x}$. (*b*) Vertical meso-scale normal stress, $P_{s,meso,y}$. (*c*) Meso-scale viscosity, $\mu_{s,meso}$.

the drag force model described in table 1 can be rewritten formally in terms of the terminal velocity and Richardson–Zaki: exponent (*n*):

$$\boldsymbol{f} = \beta(\boldsymbol{u} - \boldsymbol{v}), \quad \beta = \frac{(\rho_s - \rho_g)g\phi}{v_t(1 - \phi)^{n-2}},$$

with *n* assuming values of 4.65 and 2.325 at the two limits, respectively. When this is cast in dimensionless form, the only dimensionless group which will appear in this term is $(\Delta\rho)/\rho_s$, which is close to unity in the gas–solid flow problems. At intermediate values of Re_g and a drag model as in table 1, Fr_p does appear in the dimensionless interphase drag force term. However, it is easy to argue that its influence is quite weak for modest changes in Fr_p.

(ii) It appears through the kinetic theory viscosity (μ), conductivity (λ) and the terms representing generation and dissipation of PTE, see table 1. Our computational experiments suggest that the effect of dimensionless particle size on the meso-scale characteristics through the second route is also weak.

This is illustrated in table 5, where we have presented various average quantities for three different values of Fr_p and a fixed value of Fr_h. In these simulations, Re_p is

Fr_p	97.19	64.79	48.59
W_{slip}	1.46	1.46	1.48
T	0.018	0.018	0.021
$P_{s,KT}$	0.0023	0.0022	0.0026
$P_{s,meso,x}$	0.032	0.032	0.030
$P_{s,meso,y}$	0.015	0.015	0.017

TABLE 5. Effect of Fr_p on dimensionless domain-averaged quantities obtained from two-dimensional simulations. $Fr_h = 0.486$; $Re_p = 1.18$; $A = 4$. Average solids volume fraction = 0.05. Here, subscripts x and y denote the horizontal and vertical directions, respectively. Resolution: 16×64.

still $O(1)$. This demonstrates that the effect of particle size (dimensional quantity) is felt largely through its effect on settling velocity (dimensional quantity) and how it changes the value of Fr_h (for a given dimensional box width).

In typical riser flows, the mass loading of particles is much larger than unity, and consequently gas-phase inertia plays only a secondary role; in this regime of flow, the density ratio also has only a small influence on the meso-scale structures. The Reynolds number appears in the model only through the drag correlation and as such its effect is felt primarily via the terminal velocity. Therefore, its direct influence on the meso-scale structures is minimal.

Therefore, the average values of various quantities are determined largely by the values of ϕ, A, Fr_h and $\tilde{\gamma}$. As discussed earlier, for sufficiently large A (which is typically the case in almost all riser flow simulations), the average quantities are only weakly dependent on A, leaving ϕ, Fr_h and $\tilde{\gamma}$ as the main parameters.

We have carried out a limited number of two-dimensional simulations to explore the effect of Fr_h on slip velocity, granular temperature, meso-scale normal stresses and viscosity, and the results are summarized in figure 18(a–e). (A typical range of Fr_h relevant in riser simulations is 0.05–1.0, with the explored range of 0.2–0.5 being more common.) In the range of volume fractions shown in this figure, the granular temperature, meso-scale stresses and meso-scale viscosity clearly increase with particle volume fraction. In contrast, the effective slip velocity reveals a more complex dependence, which can be easily traced to the fact that the particle volume fraction at which the maximum slip velocity occurs (e.g. see figure 7 or 12) changes with Fr_h.

All the data shown in figure 18, with the exception of those shown as filled symbols, suggest that, as the domain size increases ($Fr_h \to 0$), the effects of the meso-scale structures reach finite asymptotic values. Physically, the existence of such limits may be interpreted as the saturation of quantities, such as velocity variance and correlation time, that characterize the meso-scale structures. On the other hand, the data shown as filled symbols suggest a more complex Fr_h scaling. Many more simulations need to be performed before the Fr_h-dependence of all of these quantities can be determined with confidence.

6. Summary

Meso-scale structures that take the form of clusters and strands, which have been observed in gas–particle flows, can be captured qualitatively through transient integration of continuum equations for the gas and particle phases. These structures arise as a result of two instability mechanisms, both of which are accounted for in a
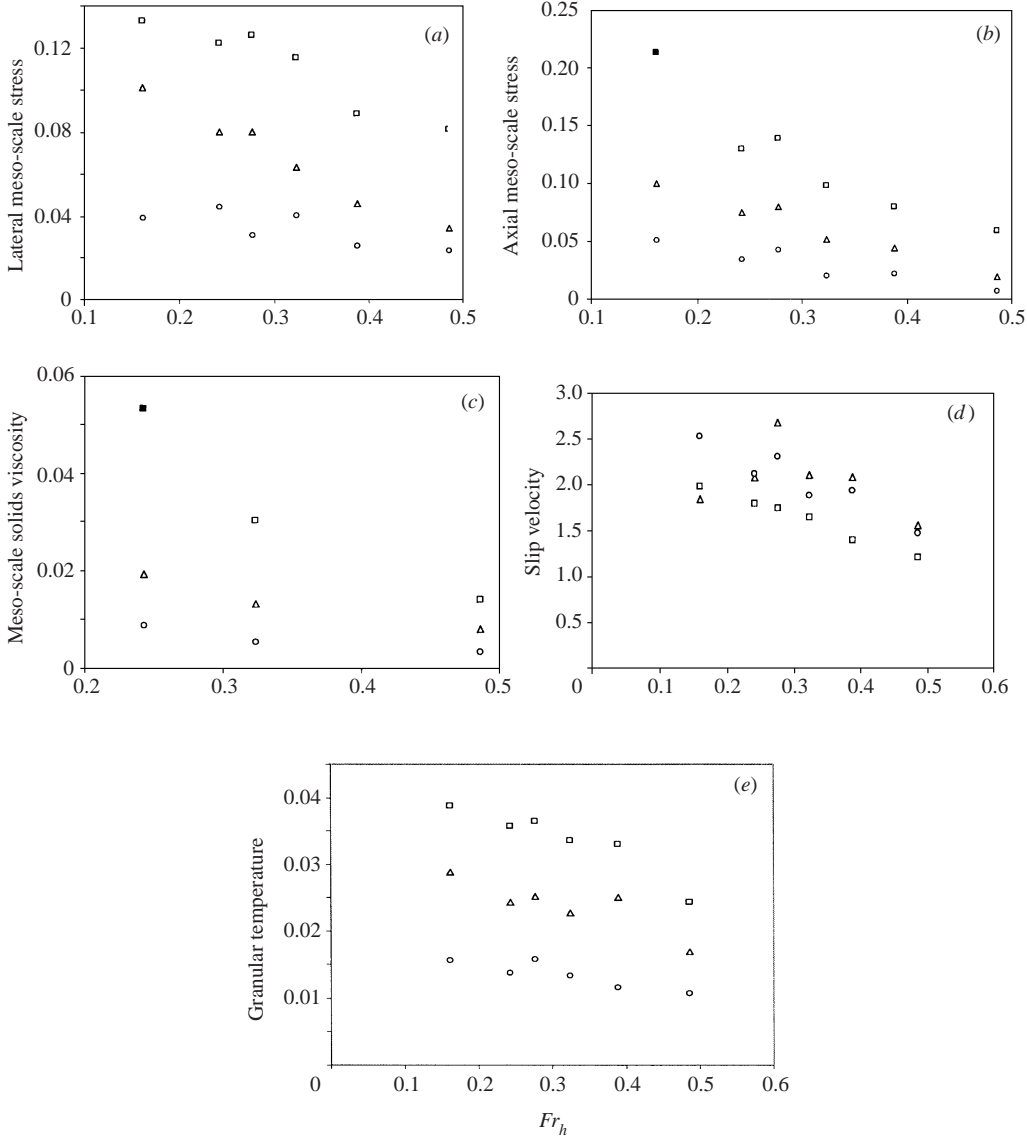
FIGURE 18. Effect of Fr_h on domain-averaged quantities. $e_p = 0.9$; $Fr_p = 64.8$; $Re_p = 1.18$; two-dimensional. Aspect ratio 1:4. Resolution: 16×64. $\bigcirc$, $\bar{\phi} = 0.025$; $\triangle$, $\bar{\phi} = 0.05$; $\square$, $\bar{\phi} = 0.10$. No macro-scale shear was imposed. (*a*) Slip velocity. (*b*) Granular temperature. (*c*) Horizontal meso-scale normal stress, $P_{s,meso,x}$. (*d*) Vertical meso-scale normal stress, $P_{s,meso,y}$. (*e*) Meso-scale viscosity of the solid phase, $\mu_{s,meso}$.

rheological model deduced in the literature by adapting the kinetic theory of gases to gas–particle mixtures. These meso-scale structures are too small to be resolved in simulations of flow in large process vessels, and are invariably invisible in the coarse-grid simulations. Yet, they affect the flow characteristics profoundly; in particular, they alter the effective interaction force that couples the gas and particle phases, and dramatically increase the effective viscosities of the two phases and the normal stresses in the particle phase. In this paper, we have presented examples to illustrate these points.

In large-eddy simulations of turbulent flow of an incompressible single-phase fluid, the sub-grid structure is sustained through macroscopic shear. In the gas–solid flow problem studied here, sub-grid-scale structure arises spontaneously through a sub-grid-scale instability and can be sustained even in the absence of macro-scale shear. We have taken a closer look at instability-driven sub-grid structure and have shown that it does alter the effective drag, viscosities and particle-phase pressure appreciably. We have also presented some calculations which include the effect of macro-scale shear. These results suggest that at low shear rates the sub-grid-scale structure and fluctuations are influenced predominantly by the sub-grid instability and not the macro-scale shear. At higher shear rates, the macro-scale shear alters the fluctuation characteristics substantially by serving to align the meso-scale structure in the axial direction. This leads to a highly anisotropic meso-scale normal stress and a shear-thinning behaviour. Our work demonstrates the need for a sub-grid model to account for the effect of the sub-grid structure, and also outlines a possible approach to developing such a model.

We close by reiterating the practical value of the present line of investigation. Coarse-grid simulation of multiphase flows is highly desirable for exploring the effects of choices made in process design/redesign, as it allows us to analyse the problem with a manageable number of spatial nodes which, in turn, permits much larger time steps to be taken when compared to the simulations with very high spatial resolution (since the maximum time step is related to the grid size through a Courant instability criterion). At the same time, the results of a coarse-grid simulation that ignores the sub-grid processes cannot be trusted as true solutions of the model equations for rapid gas–particle flows one is trying solve. Given the complex nature of the sub-grid processes, it appears doubtful if simple extensions of classical K–ε models will be able to account for the effect of meso-scale structures discussed here. Thus, a physically sound sub-grid model is not simply interesting, but is a must.

Appendix

Consider, for illustration, a two-dimensional simulation of gas–particle flow in a vertical riser. Let us suppose that we discretize the domain using equally sized, but coarse, grids. Let us further suppose that the system of equations given in table 1 is the *microscopic* model we wish to simulate. The continuity and momentum balance equations of the corresponding coarse-grid model, obtained by Favre averaging over the meso-scale (sub-grid) structures, will have a form identical to equations (1)–(4) in table 1, but σ_s, σ_g, and $\boldsymbol{f}$ appearing in these equations will be replaced by σ_s^*, σ_g^* and $\boldsymbol{f}^*$, representing the effective quantities.

In order to construct a simple sub-grid model for the effect of meso-scale structures resulting from sub-grid-scale instabilities, one can perform highly resolved simulations of the type described in the text in a doubly periodic domain whose size is exactly the same as the grid size of the coarse-grid simulation. Such simulations are performed for various mean solids volume fractions and various shear rates. The results are then used to compute effective slip velocity, $\boldsymbol{P}_{s,meso}$, $\mu_{s,meso}$ and $\mu_{app,g}$ as functions of the mean solids volume fraction and shear rates.

The slip velocity data are then correlated, as illustrated in figure 6 for the case $\gamma = 0$. One can then write an effective drag law of the form

$$\boldsymbol{f}^* = \beta^*(\boldsymbol{u} - \boldsymbol{v}), \quad \beta^* = \frac{(\rho_s - \rho_g)g(1 - \phi)\phi}{v_t F_1(\phi)}. \tag{A 1}$$

Similar calculations can be performed at various shear rates to include the effect of shear.

As described in the text, solid-phase stress induced by the meso-scale fluctuations is significantly larger than the kinetic theory stress and so the latter can be neglected. This, of course, does *not* mean that the kinetic theory stress plays no role in the macro-scale features of gas–particle flow. It simply means that the primary role of the stress due to the micro-scale fluctuations, captured by the kinetic theory, is confined to the sub-grid processes; these micro-scale fluctuations control the meso-scale structure and, therefore, appear indirectly in the macro-scale through the solid-phase stress induced by the meso-scale fluctuations. A simple model for $\boldsymbol{\sigma}_s^*$ is then written as

$$\boldsymbol{\sigma}_s^* = \boldsymbol{P}_{s,meso} - 2\mu_{s,meso}\boldsymbol{S},$$

which is similar in form to that used by Tsuo & Gidaspow (1989). $\boldsymbol{P}_{s,meso}$ (a diagonal tensor) and $\mu_{s,meso}$ are empirical expressions obtained by fitting the data obtained in the highly resolved simulations alluded to above. The expressions should account for the dependence on the solids volume fraction and the rate of deformation.

Following the same approach, we can express $\boldsymbol{\sigma}_g^*$ as

$$\boldsymbol{\sigma}_g^* = p_g\boldsymbol{I} - 2\mu_{app,g}\boldsymbol{S}_g$$

where p_g is simply the gas pressure, $\mu_{app,g}$, and will depend on the solids volume fraction and the rate of deformation.

In this simple model, it is not necessary to include the PTE balance in the coarse-grid simulations, as long as the grid size is sufficiently large that the PTE balance is relevant only at the sub-grid level.

Note that such an approach focuses on time-averaged (sub-grid-scale) quantities, which fluctuate rapidly around a statistical mean (e.g. see figure 3). Time-averaged quantities suffice only if a complete separation of scales exists between the meso- and macro-scales. Figure 3 suggests that such a separation of scales may not exist, and so it is possible that the fluctuating nature of the interphase interaction force and the effective stresses must be accounted for in coarse-grid simulations. Recall that, in our problem, instabilities begin at a small scale and grow to larger scales. Introducing (stochastic) terms to capture the fluctuating nature of the interphase interaction force and the effective stresses (arising from spatio-temporal meso-scale structures) may allow us to initiate and sustain fluctuations in coarse-grid simulations.

It appears reasonable to retain the inflow and outflow boundary conditions that are currently used in CFD simulations. At bounding walls, the normal velocity of the two phases should obviously equal that of the wall. Wall boundary conditions for the tangential components of gas and particle velocities, suitable for coarse-grid simulations, remain a challenge. Nevertheless, for the specific problem of gas–particle flow in wide risers, it seems adequate to use simple free-slip boundary conditions for both phases, as the wall resistance is known to contribute only minimally.

It is straightforward to extend this idea to three-dimensional simulations with equally sized grids.

When the grids are unequally sized, the approach outlined here becomes much harder, as one now has to do highly resolved simulations for large number of domain

sizes. This clearly shows why a more elegant and fundamentally based sub-grid model that explicitly accounts for the coarse grid size, and does not require the highly resolved simulations, must be developed.

REFERENCES

AGRAWAL, K. 2000 The role of meso-scale structures in rapid gas-solid flows. PhD Dissertation, Princeton University.

ANDERSON, T. B. & JACKSON, R. 1967 Fluid mechanical description of fluidized beds. Equations of motion. *Indust. Engng Chem. Fundam.* **6**, 527–539.

ANDERSON, K., SUNDARESAN, S. & JACKSON, R. 1995 Instabilities and the formation of bubbles in fluidized beds. *J. Fluid Mech.* **303**, 327–366.

BADER, R., FINDLAY, J. & KNOWLTON, T. M. 1988 Gas/solid flow patterns in a 30.5 cm diameter circulating fluidized bed. In *Circulating Fluidized Bed Technology II* (ed. P. Basu & J. F. Large), pp. 123–137. Pergamon.

BALZER, G., BOELLE, A. & SIMONIN, O. 1995 Eulerian gas-solid flow modelling of dense fluidized beds. In *Fluidization VIII*, p. 1125.

BOELLE, A., BALZER, G. & SIMONIN, O. 1995 Gas-solid flows. In *Gas-particle Flows*. ASME FED, vol. 228, p. 9.

BOLIO, E. & SINCLAIR, J. 1995 Gas turbulence modulation in the pneumatic conveying of massive particles in vertical tubes. *Intl J. Multiphase Flow* **21**, 985–1001.

BOUILLARD, J. X., LYCZKOWSKI, R. W. & GIDASPOW, D. 1989 Porosity distributions in a fluidized bed with an immersed obstacle. *AIChE J.* **35**, 908–922.

DASGUPTA, S., JACKSON, R. & SUNDARESAN, S. 1994 Turbulent gas–particle flow in vertical risers. *AIChE J.* **40**, 215–228.

ENWALD, H. & ALMSTEDT, A. E. 1999 Fluid dynamics of a pressurized fluidized bed: comparison between numerical solutions from two-fluid models and experimental results. *Chem. Engng Sci.* **54**, 32–342.

ENWALD, H., PEIRANO, E. & ALMSTEDT, A. E. 1997 Eulerian two-phase theory applied to fluidization. *Intl J. Multiphase Flow* **22**, Suppl., 21–66.

ENWALD, H., PEIRANO, E., ALMSTEDT, A. E. & LECKNER, B. 1999 Simulation of the fluid dynamics of a bubbling fluidized bed. Experimental validation of the two-fluid model and evaluation of a parallel multiblock solver. *Chem. Engng Sci.* **54**, 31-328.

FERZIGER, J. H. & PERI, M. 1996 *Computational Methods for Fluid Dynamics*. Springer.

GIDASPOW, D. 1993 Hydrodynamic modelling of circulating and bubbling fluidized beds. In *Particulate Two-Phase Flow* (ed. M. C. Roco), pp. 778–810. Butterworth-Heinemann.

GIDASPOW, D. 1994 *Multiphase Flow and Fluidization*, pp. 31–58, 197–238. Academic.

GLASSER, B. J., KEVREKIDIS, I. G. & SUNDARESAN, S. 1996 One- and two-dimensional travelling wave solutions in gas-fluidized beds. *J. Fluid Mech.* **306**, 183–221.

GLASSER, B. J., KEVREKIDIS, I. G. & SUNDARESAN, S. 1997 Fully developed travelling wave solutions and bubble formation in fluidized beds. *J. Fluid Mech.* **334**, 157–188.

GLASSER, B.J., SUNDARESAN, S. & KEVREKIDIS, I.G. 1998 From bubbles to clusters in fluidized beds. *Phys. Rev. Lett.* **81**, 1849–1852.

GOLDHIRSCH, I., TAN, M.-L. & ZANETTI, G. 1993 A molecular dynamical study of granular fluids I: The unforced granular gas in two dimensions. *J. Sci. Comput.* **8**, 1–40.

GRACE, J. R. & TUOT, J. 1979 A theory for cluster formation in vertically conveyed suspensions of intermediate density. *Trans. Inst. Chem. Engrs* **57**, 49–54.

HOOMANS, B. P. B., KUIPERS, J. A. M., BRIELS, W. J. & VAN SWAAIJ, W. P. M. 1996 Discrete particle simulation of bubble and slug formation in a two-dimensional gas-fluidized bed: A hard-sphere approach. *Chem. Engng Sci.* **51**, 99–108.

HOPKINS, M. A. & LOUGE, M. Y. 1991 Inelastic microstructure in rapid granular flows of smooth disks. *Phys. Fluids* A **3**, 47–57.

HORIO, M. 1995 Cluster and agglomerate formation in fluidized suspensions. *Proc. 2nd Intl Conf. on Multiphase Flows, Kyoto, 3–7 April 1995*, vol. 3 (ed. A. Serizawa, T. Fukano & J. Bataille), FB1-1.

HRENYA, C. M. & SINCLAIR, J. L. 1997 Effects of particle-phase turbulence in gas-solid flows. *AIChE J.* **43**, 853–869.

ITO, M., TSUKADA, M., SHIMAMURA, J. & HORIO, M. 1998 Prediction of cluster size and slip velocity in circulating fluidized beds by a DSMC model. In *Fluidization IX* (ed. L.-S. Fan & T. M. Knowlton), pp. 526–532. Engineering Foundation Publication.

JENKINS, J. T. 1992 Boundary conditions for rapid granular flow: Flat, frictional wall. *Trans ASME: J. Appl. Mech.* **114**, 120–127.

JENKINS, J. T. & LOUGE, M. Y. 1997 On the flux of fluctuation energy in a collisional grain flow at a flat, frictional wall. *Phys. Fluids* **9**, 2835–2840.

JENKINS, J. T. & RICHMAN, M. W. 1985 Grad's 13-moment system for a dense gas of inelastic spheres. *Arch. Rat. Mech. Anal.* **87**, 355–377.

JENKINS, J. T. & RICHMAN, M. W. 1986 Boundary conditions for plane flows of smooth, nearly elastic circular disks. *J. Fluid Mech.* **171**, 53–69.

JOHNSON, P. C. & JACKSON, R. 1987 Frictional-collisional constitutive relations for granular materials, with applications to plane shearing. *J. Fluid Mech.* **130**, 187–202.

KOCH, D. L. 1990 Kinetic theory for a monodisperse gas-solid suspension. *Phys. Fluids* A **2**, 1711–1723.

KOCH, D. L. & SANGANI, A. S. 1999 Particle pressure and marginal stability limits for a homogeneous monodisperse gas fluidized bed: kinetic theory and numerical simulations. *J. Fluid Mech.* **400**, 229–263.

KUDROLLI, A. & GOLLUB, J. P. 1997 Studies of cluster formation due to collisions in granular material. *Powders & Grains 97* (ed. R. Behringer & J. Jenkins), pp. 535–538. Balkema, Rotterdam.

LOUGE, M., MASTORAKOS, E. & JENKINS, J. T. 1991 The role of particle collisions in pneumatic transport. *J. Fluid Mech.* **231**, 345–359.

LUN, C. K. K., SAVAGE, S. B., JEFFREY, D. J. & CHEPURNIY, N. 1984 Kinetic theories of granular flows: inelastic particles in Couette flow and slightly inelastic particles in a general flow field. *J. Fluid Mech.* **140**, 223–256.

MA, D. & AHMADI, G. 1988 A kinetic model for rapid granular flows of nearly elastic particles including interstitial fluid effects. *Powder Technol.* **56**, 191–207.

MCNAMARA, S. & YOUNG, W. R. 1996 Dynamics of a freely evolving two-dimensional granular medium. *Phys. Rev.* B **53**, 5089–5100.

NIEUWLAND, J. J., ANNALAND M. V., KUIPERS, J. A. M. & VAN SWAAIJ, W. P. M. 1996 Hydrodynamic modelling of gas/particle flows in riser reactors. *AIChE J.* **42**, 1569–1582.

NIEUWLAND, J. J., HUIZENGA, J. J. P., KUIPERS, J. A. M. & VAN SWAAIJ, W. P. M. 1995 Hydrodynamic modelling of circulating fluidized beds. *Chem. Engng Sci.* **49**, 5803–5811.

NOTT, P. R., ALAM, M. A., AGRAWAL, K., JACKSON, R. & SUNDARESAN, S. 1999 The effect of boundaries on the plane Couette flow of granular materials: a bifurcation analysis. *J. Fluid Mech.* **397**, 203–229.

O'BRIEN, T. J. & SYAMLAL, M. 1994 Particle cluster effects in the numerical simulation of a circulating fluidized bed. In *Circulating Fluidized Bed Technology IV* (ed. A. A. Avidan), pp. 345–350. The Secretariat of the International Conference on Circulating Fluid Beds.

OUYANG, J. & LI, J. 1999 Discrete simulation of heterogeneous structure and dynamic behavior in gas-solid fluidization. *Chem. Engng Sci.* **54**, 5427–5440.

PITA, J. A. & SUNDARESAN, S. 1991 Gas-solid flow in vertical tubes. *AIChE J.* **37**, 1009–1018.

PITA, J. A. & SUNDARESAN, S. 1993 Developing flow of a gas–particle mixture in a vertical riser. *AIChE J.* **39**, 541–552.

RICHARDSON, J. F. & ZAKI, W. N. 1954 Sedimentation and fluidization: Part I. *Trans. Inst. Chem. Engrs* **32**, 35–53.

SAMUELSBERG, A. & HJERTAGER, B. 1996 Computational modelling of gas/particle flow in a riser. *AIChE J.* **42**, 1536–1546.

SAVAGE, S. B. 1992 Instability of unbounded uniform granular shear flow. *J. Fluid Mech.* **241**, 109–123.

SCHNITZLEIN, M. G. & WEINSTEIN, H. 1988 Flow characterization in high-velocity fluidized beds using pressure fluctuations. *Chem. Engng Sci.* **43**, 2605–2614.

SINCLAIR, J. L. & JACKSON, R. 1989 Gas-particle flow in a vertical pipe with particle-particle interaction. *AIChE J.* **35**, 1473–1486.

Smagorinsky, J. 1963 General circulation experiments with the primitive equations: Part I, the basic experiment. *Mon. Wea. Rev.* **91**, 99–164.

Srivastava, A., Agrawal, K., Sundaresan, S., Reddy Karri, S. B. & Knowlton, T. M. 1998 Dynamics of gas–particle flow in circulating fluidized beds. *Powder Technol.* **100**, 173–182.

Syamlal, M. 1998 *MFIX Documentation: Numerical Techniques.* DOE/MC-31346-5824. NTIS/DE98002029.

Syamlal, M. Rogers, W. & O'Brien, T. J. 1993 *MFIX Documentation.* US Department of Energy, Federal Energy Technology Center, Morgantown.

Tan, M.-L. 1995 Micro-structures and macro-structures in rapid granular flow. PhD dissertation, Princeton University.

Tan, M.-L. & Goldhirsch, I. 1997 Intercluster interactions is rapid granular shear flows. *Phys. Fluids* **9**, 856–869.

Tanaka, T., Yonemura, S., Kiribayashi, K & Tsuji, Y. 1996 Cluster formation and particle-induced instability in gas-solid flows predicted by the DSMC method. *JSME Intl J.* B **39**, 239–245.

Tanaka, T., Yonemura, S. & Tsuji, Y. 1995 Effects of particle properties on the structure of clusters. In *Gas-particle Flows.* ASME FED, vol. 228, pp. 297–302.

Tsuji, Y., Kawaguchi, T. & Tanaka, T. 1993 Discrete particle simulation of two-dimensional fluidized bed. *Powder Technol.* **77**, 79–87.

Tsuji, Y., Tanaka, T. & Yonemura, S. 1998 Cluster patterns in circulating fluidized beds predicted by numerical simulation: Discrete particle model vs. two-fluid model. *Powder Technol.* **95**, 254–264.

Tsukada, M. 1995 Fluidized bed hydrodynamics, heat transfer and high temperature process developments. PhD Dissertation, Tokyo University of Agriculture and Technology, Tokyo, Japan.

Tsuo, Y. P. & Gidaspow, D. 1990 Computation of flow patterns in circulating fluidized beds. *AIChE J.* **36**, 885–896.

Weinstein, H., Shao, M. & Schnitzlein, M., 1986 Radial variation in solid density in high velocity fluidization. In *Circulating Fluidized Bed Technology I* (ed. P. Basu), pp. 201–206. Pergamon.

Wen, C. Y. & Yu, Y. H. 1966 Mechanics of Fluidization. *Chem. Engng Prog. Symp. Ser.* **62**, 100–111.

Wilhelm, R. H. & Kwauk, M. 1948 Fluidization of solid particles. *Chem. Engng. Prog.* **44**, 201–218.

Wylie, J. J. & Koch, D. L. 2000 Particle clustering due to hydrodynamic interactions. *Phys. Fluids* **12**, 964–970.

Yasuna, J., Moyer, H., Elliot, S. & Sinclair, J. 1995 Quantitative predictions of gas–particle flow in a vertical pipe with particle-particle interactions. *Powder Technol.* **84**, 23–34.

Zhang, J., Jiang, P. & Fan, L.-S. 1998 Flow behaviour in transients of solid flow rates in a circulating fluidized bed system. In *Fluidization IX* (ed. L.-S. Fan & T. M. Knowlton). Engineering Foundation Publication.